



Factors controlling the interannual variation of 30–60-day boreal summer intraseasonal oscillation over the Asian summer monsoon region

Jiaying Li¹ · Jianguo Mao² 

Received: 28 March 2017 / Accepted: 18 April 2018 / Published online: 25 April 2018
© Springer-Verlag GmbH Germany, part of Springer Nature 2018

Abstract

The 30–60-day boreal summer intraseasonal oscillation (BSISO) is a dominant variability of the Asian summer monsoon (ASM), with its intensity being quantified by intraseasonal standard deviations based on OLR data. The spatial and interannual variations of the BSISO intensity are identified via empirical orthogonal function (EOF) analysis for the period 1981–2014. The first EOF mode (EOF1) shows a spatially coherent enhancement or suppression of BSISO activity over the entire ASM region, and the interannual variability of this mode is related to the sea surface temperature anomaly (SSTA) contrast between the central–eastern North Pacific (CNP) and tropical Indian Ocean. In contrast, the second mode (EOF2) exhibits a seesaw pattern between the southeastern equatorial Indian Ocean (EIO) and equatorial western Pacific (EWP), with the interannual fluctuation linked with developing ENSO events. During strong years of EOF1 mode, the enhanced low-level westerlies induced by the summer-mean SSTA contrast between the warmer CNP and cooler tropical Indian Ocean tend to form a wetter moisture background over the eastern EIO, which interacts with intraseasonal low-level convergent flows, leading to stronger equatorial eastward propagation. The intensified easterly shear favors stronger northward propagation over the South Asian and Eastern Asian/Western North Pacific sectors, respectively. Opposite situation is for weak years. For interannual variations of EOF2 mode, the seesaw patterns with enhanced BSISO activity over the southeastern EIO while weakened activity over the EWP mostly occur in the La Niña developing summers, but inverse patterns appear in the El Niño developing summers.

Keywords Boreal summer intraseasonal oscillation · Interannual variation · Multi-scale interaction

1 Introduction

The Asian summer monsoon (ASM) is the largest monsoon system on the globe, affecting approximately 60% of the world's population. This huge monsoon system can be divided into two subsystems, the South Asian summer monsoon (SASM) and the Eastern Asian/Western North Pacific (EA/WNP) monsoon (Tao and Chen 1987). The considerable variability of the ASM on a wide range of timescales

(Webster et al. 1998) leads to severe disasters, such as floods and droughts as well as secondary landslides and mudslides, frequently hit this monsoon region, causing hardship and suffering for millions of people and significant economic loss. Therefore, it is vital to study the mechanisms behind anomalous ASM conditions. Moreover, the ASM also significantly affects weather and climate in other regions (Tong et al. 2009; Trenberth 2011; Li et al. 2014). As a result, the ASM is always a key topic in both weather and climate studies. Within the annual cycle, intraseasonal oscillation (ISO) is an important variability of the ASM (Hoyos and Webster 2007; Li and Zhou 2015). The ISOs of the ASM can modulate tropical cyclone activity over both the tropical Indian Ocean and WNP (Liebmann et al. 1994; Maloney and Hartmann 2000; Mao and Wu 2010; Hsu and Li 2011) and also lead to large-scale seasonal-mean rainfall anomalies (Zhu et al. 2003; Bhat 2006; Ding and Wang 2009; Li et al. 2015). Furthermore, as ISOs are the main source of predictability

✉ Jianguo Mao
mjm@lasg.iap.ac.cn

¹ China University of Geosciences, Wuhan 430074, China

² State Key Laboratory of Numerical Modeling for Atmospheric Sciences and Geophysical Fluid Dynamics (LASG), Institute of Atmospheric Physics, Chinese Academy of Sciences, P. O. Box 9804, Beijing 100029, China

for extended-range forecasts, studying ISOs, especially the boreal summer ISOs (BSISOs) over the ASM area, is critical for achieving seamless weather-to-climate prediction.

BSISOs over the ASM region have two dominant periods, 30–60 and 10–20 days (e.g., Lawrence and Webster 2002; Mao and Chan 2005). The 30–60-day BSISO is a propagating convection–circulation coupled system, characterized by a prominent baroclinic structure (Mao et al. 2010; Lee et al. 2013). Compared with its wintertime counterpart, the Madden–Julian oscillation (MJO; Madden and Julian 1971, 1972), which mainly propagates eastward along the equator, the 30–60-day BSISO over the ASM region has a more complex propagation pattern. The anomalous convection signal of the 30–60-day BSISO originates in the equatorial Indian Ocean (EIO; 5°S–5°N, 60°–100°E) (Wang and Rui 1990; Jones et al. 2004) and then propagates eastward along the equator as it grows (Wang and Xie 1997). When the 30–60-day BSISO reaches the equatorial eastern Indian Ocean (EEIO; 5°S–5°N, 90°–100°E), it splits off, with a component moving poleward in the form of a Rossby wave-like pattern toward the Indian Subcontinent and Bay of Bengal, thus leading to a north–south oriented dipole pattern along the Indian Ocean meridians. The anomalous rainfall associated with the 30–60-day BSISO develops further after moving into the equatorial western Pacific (EWP; 5°S–5°N, 110°–140°E) and then propagates northward/northwestward into the South China Sea–WNP (SCS–WNP). The northward propagation along the western Pacific longitudes similarly gives rise to a north–south oriented dipole pattern between the EWP and SCS–WNP. Note that the equatorial eastward propagation from the EIO to the EWP connects the north–south oriented dipole pattern over the SASM region with the complementary dipole pattern over the EA/WNP sector in most cases (e.g., Annamalai and Sperber 2005), thus forming a typical quadrupole pattern over the entire ASM area (Kemball-Cook and Wang 2001; Annamalai and Sperber 2005; Seo et al. 2007; Lee et al. 2013).

The 10–20-day BSISO over the ASM region is characterized by an elongated and front-like circulation structure aligned southwest–northeast with westward propagation over the tropical Indian Ocean and northwestward propagation over the WNP (e.g., Mao and Chan 2005; Zhou and Chan 2005). Thus, it differs significantly from the 30–60-day BSISO in terms of both flow pattern and propagation.

Both BSISO modes over the ASM area experience significant interannual variation. Qi et al. (2008) suggested that the intensity of the 30–60-day BSISO over the SASM region depends on the phase of El Niño and Southern Oscillation (ENSO) events, with a stronger 30–60-day BSISO during summers with developing El Niño and weaker 30–60-day BSISO during summers with decaying El Niño. Lin and Li (2008) found that the propagation features of the 30–60-day BSISO are also closely associated with ENSO evolution.

During El Niño developing summers, both the equatorial eastward and the northward propagation over the EA/WNP region are enhanced significantly, while the opposite situation occurs during El Niño decaying summers. The recent work of Wu and Cao (2016) has suggested that ENSO has significant influence on the intensity of both the 10–20- and 30–60-day BSISOs over the tropical western Pacific, with enhanced 10–20-day BSISO during El Niño developing summers, but stronger 30–60-day BSISO during La Niña decaying summers. The Indian Ocean Dipole (IOD; Saji et al. 1999) is another tropical air–sea coupled mode that strongly affects BSISO behavior on interannual timescales. Ajayamohan et al. (2008) noted that the IOD evidently influences the intensity and propagation features of 30–60-day BSISOs over the SASM region, with strong (weak) BSISO propagating coherently (incoherently) northward from 5°S to 20°N during negative (positive) IOD years.

The periodicity of the BSISO over the SCS also exhibits its significant interannual variation (Mao and Chan 2005), with the relative importance of the 30–60- and 10–20-day BSISOs varying from year to year. Kajikawa and Yasunari (2005) found that, over the SCS, the 10–20-day BSISO is relatively strong (weak) when the 30–60-day counterpart is suppressed (enhanced) during July–September. Yang et al. (2008) further confirmed the anti-correlation relationship between the intensities of the 10–20- and 30–60-day BSISOs over the SCS. Recently, Liu et al. (2016) have attributed the interannual variation of BSISO periodicity over the SCS–WNP to the summertime sea surface temperature anomalies (SSTAs) over the equatorial central–eastern Pacific. Anomalous cooling (warming) in the equatorial central–eastern Pacific during summer tends to weaken (strengthen) the low-level moisture and easterly vertical shear over the WNP, thus suppressing (enhancing) the development of the 10–20-day BSISO. Meanwhile, strong ascending (descending) motion over the Maritime Continent favors (impedes) the 30–60-day BSISO that originates over the EIO propagating continually across the Maritime Continent into the EWP. Therefore, the 30–60-day (10–20-day) BSISO dominates over the WNP during cooling (warming) episodes of the equatorial central–eastern Pacific.

Note that only the interannual variations of the BSISOs over particular monsoon areas, such as the SCS, WNP or SASM region, have been investigated in previous studies, while the interannual variability of the BSISOs over the entire ASM region remains elusive. As the BSISO over the entire ASM area is an integrated system on both 10–20- and 30–60-day time-scales (e.g., Annamalai and Slingo 2001; Lee et al. 2013), the relationship between the interannual variation of BSISO over the SASM and EA/WNP regions requires investigation. Note also that the BSISOs are dynamically interpreted as tropical propagating wave envelope with multi-scale structure, indicating that multi-scale interaction

processes play an important role in the evolution of the BSISOs (Jiang et al. 2004; Li et al. 2009; Hsu and Li 2011; Li and Zhou 2015). Previous studies revealed only the modulation of BSISOs by the ENSO/IOD-related seasonal-mean circulation anomalies. The specific seasonal-mean–BSISO interaction processes that explain the modulation of the interannual variability of BSISOs deserve further study.

As the 10–20- and 30–60-day BSISO modes are distinct (e.g., Lee et al. 2013), the interannual variability of these two BSISO modes should be discussed separately. Note that the 30–60-day mode explains more BSISO variability (40%) than the 10–20-day counterpart (25%) over the ASM area (not shown), indicating that the interannual variation of BSISO over the ASM region is more attributed to the interannual variability of the 30–60-day component. Therefore, in this paper, we focus on the interannual variability of the 30–60-day BSISO. For brevity, the 30–60-day BSISO will be simply referred to as BSISO in the following sections. The objective of the current study is to investigate the spatial and interannual variability of the BSISO activity over the entire ASM region and to reveal physical mechanisms responsible for the interannual variations of the leading modes in BSISO intensity.

Section 2 briefly describes the data and statistical methods. Section 3 identifies the spatio-temporal variability of BSISO activity over the ASM region. Section 4 studies the interannual variability of the first EOF mode of BSISO intensity. Section 5 analyzes interannual variation of the second EOF mode. Section 6 reveals external forcing relating to interannual variations of the two leading modes. Finally, a summary and discussion are given in Sect. 7.

2 Data and methods

2.1 Data

Daily outgoing longwave radiation (OLR) data from the National Oceanic and Atmospheric Administration (NOAA) polar-orbiting satellites are often used as a good proxy for the tropical deep convection (Liebmann and Smith 1996), and are available from 1974 to 2017. Pentad precipitation data from the Global Precipitation Climatology Project (GPCP) (Huffman et al. 2001) can also represent tropical convection well and are available from 1979 to 2014, with a horizontal resolution of $2.5^\circ \times 2.5^\circ$. We compare the representation of BSISO activity in the OLR and GPCP precipitation data and find that the representation of GPCP rainfall is highly consistent with that of OLR (see details in Sect. 3). Since the daily OLR can better capture the large scale variation of tropical convection, this dataset is used to define the interannual variation index of BSISO through empirical orthogonal function (EOF) analysis, so as to depict clearly

the interannual variation of BSISO intensity over the ASM region from 1981 to 2014.

Daily atmospheric circulation data including three-dimensional wind components and relative humidity are extracted from the Japanese 55-year Reanalysis project conducted by the Japan Meteorological Agency (Kobayashi et al. 2015). This atmospheric reanalysis product has a horizontal resolution of $1.25^\circ \times 1.25^\circ$, with 37 levels in the vertical. To depict the BSISO-related oceanic conditions, daily SSTs are derived from the NOAA Optimum Interpolation 1/4 Degree Daily Sea Surface Temperature (OISST) analysis (Reynolds et al. 2007) with a horizontal resolution of $0.25^\circ \times 0.25^\circ$. Both the atmospheric reanalysis and SST data cover the period 1981–2014.

2.2 Methods

Following the method of Li et al. (2015), intraseasonal anomalies for key variables (such as OLR and 850-hPa zonal winds) are obtained from daily data by the following three steps: (1) remove the seasonal cycle by subtracting the time-mean and the first three harmonics of the daily-resolved climatology; (2) remove the interannual and decadal variability by subtracting the mean of the last 120 days (Lee et al. 2013); (3) apply a 10-day running mean to the time series for each variable to remove the high-frequency components (less than 10 day). As the obtained intraseasonal anomalies contain both the 10–20- and 30–60-day signals, a Lanczos filter is then applied to extract the 30–60-day BSISO-related anomalies.

In statistics, standard deviation is a good measure used to quantify the variation of a time series. We calculated the standard deviation of the 30–60-day filtered OLR and GPCP precipitation time series at each grid cell within the ASM region (10°S – 40°N , 40° – 160°E) during each boreal summer (June–August) over 1981–2014 respectively, so as to quantify the BSISO intensity over the ASM region year by year. Deng et al. (2016) and Liu et al. (2016) also used the standard deviation of intraseasonal OLR anomalies to quantify the ISO intensity.

Because EOF decomposition is a straightforward technique to capture spatio-temporal variability, an EOF analysis is applied to the BSISO intensity matrix of the 30–60-day filtered OLR or GPCP precipitation to identify the dominant spatio-temporal modes of BSISO intensity over the ASM region. As the principal component (PC) time series of an EOF mode reflects the temporal variability of the spatial pattern, we utilize the PC time series of EOF1 and EOF2 (denoted as PC1 and PC2) derived from the 30–60-day filtered OLR anomalies to measure the year-to-year variation of BSISO intensity in the corresponding mode for the period 1981–2014. As PC1 and PC2 mostly vary on the interannual timescale, the standardized PC1 and PC2 are thus defined as

the BSISO Interannual Variation indices (BIVI1 and BIVI2). From statistical considerations of sample size, the critical threshold chosen to categorize anomalous BSISO years is 0.8 standard deviations. An anomalously strong (weak) BSISO year is thus classified as one with a BIVI1 or BIVI2 value greater than 0.8 (less than -0.8). Composite analyses of the key seasonal-mean variables (such as SST, specific humidity and surface winds) are conducted to reveal the distinctive backgrounds of the strong and weak years. The statistical significance of the composite variables is estimated by the Student's *t*-test.

To display the distinctive features of equatorial eastward propagation, wavenumber–frequency spectra of OLR and 850-hPa zonal wind intraseasonal anomalies over the equatorial region are compared for the strong and weak years. As the BSISO activity is mainly confined to the latitudinal zone 10°S – 30°N , we compare the finite domain wavenumber–frequency spectra of the intraseasonal OLR and 850-hPa zonal wind anomalies in the meridional direction over the SASM (10°S – 30°N , 60° – 100°E) and EA/WNP (10°S – 30°N , 110° – 140°E) regions for the strong and weak years, so as to reveal the interannual variations of northward propagation over the monsoon regions. Given that the evolution of OLR or 850-hPa zonal wind anomalies in the meridional direction is not cyclic, we follow Teng and Wang (2003) in applying split-cosine-bell tapering to the time series at each longitude before the Fourier transform in order to reduce spectral leakage. Latitude–lag–time correlation diagrams are also used to show differences in northward propagations between strong and weak years. The statistical significance of all the correlation coefficients is tested on the basis of two-tailed probabilities. As the time filtering usually reduces the degrees of freedom of the filtered time series, the effective sample sizes are recalculated using the method of Bretherton et al. (1990).

We conduct moisture budget diagnosis to reveal the mechanism behind the interannual variation of BSISO activity. The total moisture tendency in Eq. (1) at a constant level is determined by horizontal and vertical advection of moisture and the atmospheric apparent moisture sink Q_2 (Yanai et al. 1973):

$$\frac{\partial q}{\partial t} = -\vec{V} \cdot \nabla q - \omega \frac{\partial q}{\partial p} - \frac{Q_2}{L}, \quad (1)$$

where q is specific humidity, t is time, \vec{V} is the horizontal wind vector, p is the pressure, ω is the vertical pressure velocity, and L is the latent heat of condensation. With the continuity equation, the vertical moisture advection can be further decomposed into two terms: the horizontal moisture convergence term ($-\vec{q} \cdot \nabla \vec{V}$) and the vertical flux term ($-\frac{\partial \omega q}{\partial p}$) (Hsu and Li 2012). Therefore, the total moisture tendency may be written as

$$\frac{\partial q}{\partial t} = -\vec{V} \cdot \nabla q - q \nabla \cdot \vec{V} - \frac{\partial \omega q}{\partial p} - \frac{Q_2}{L}. \quad (2)$$

Applying the 30–60-day filtering to each term of Eq. (2), we obtain the BSISO-related moisture budget.

3 Spatial and interannual variations in BSISO activity over the ASM region

Figure 1a, b shows the spatial distributions of the first two EOF modes of the BSISO intensity (indicated by the 30–60-day filtered OLR standard deviation), with the first and second modes accounting for 13.3 and 7.9% of the total variance, respectively. According to the rule of North et al. (1982), these two modes are statistically distinguishable. The EOF1 pattern is characterized by positive loadings over both the SASM and EA/WNP regions, with four major centers located over the EIO, EWP, Indian Subcontinent–Bay of Bengal and SCS–WNP (Fig. 1a). Note that these centers are also the four key areas of the BSISO quadruple pattern over the ASM region (e.g., Lee et al. 2013). Thus, such an EOF1 pattern indicates a spatially coherent strengthening or weakening of BSISO activity over the entire ASM region. For EOF2 pattern (Fig. 1b), large negative loadings are observed over the EWP, while positive loadings are present mostly over the southeastern EIO, forming a seesaw pattern in intensity. Note that positive loadings also occur over the Arabian Sea and the WNP around 25°N (Fig. 1b).

To demonstrate the robustness of such dominant spatial patterns and their temporal variations, the same EOF analysis is applied to the standard deviations derived from the 30–60-day filtered GPCP rainfall data for the same period (1981–2014). The variances explained by the first two EOFs are 11.4 and 8.3%, respectively. These two EOF modes are also statistically distinguishable according to the method of North et al. (1982). The EOF1 structure of GPCP rainfall (Fig. 1c) also exhibits coherent positive loadings over both SASM and EA/WNP areas, almost identical to the EOF1 pattern (Fig. 1a) derived from the OLR data. Corresponding to the OLR-derived EOF2 pattern (Fig. 1b), the seesaw pattern is distinctly present around the equator in EOF2 mode of GPCP rainfall (Fig. 1d). Positive loadings can be identified over northern Arabian Sea and western Indian continent, but only weak positive loading is found over the WNP (Fig. 1d), indicating that the EOF2 mode of GPCP rainfall differs from that of OLR to some extent.

To verify that these two spatial modes derived from OLR and GPCP rainfall data are temporally consistent, we calculate the correlation coefficient between the two time series of PC1 or PC2. The correlation between PC1 time series is 0.73, and the correlation between the PC2 time series is

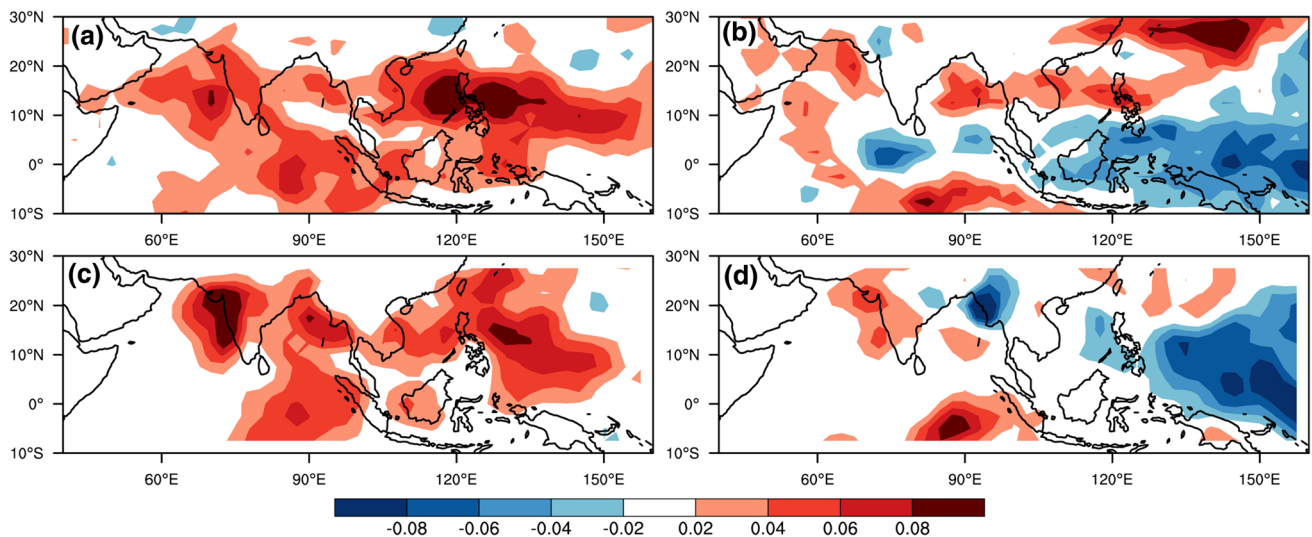


Fig. 1 Spatial distributions of the first two EOF modes of the intraseasonal standard deviations derived from the boreal summer (1 June–31 August) 30–60-day filtered OLR anomalies over the ASM region (10°S–40°N, 40°–160°E) for the period 1981–2014: **a** EOF1 and **b**

EOF2. Red and blue colors indicate positive and negative loadings, respectively. **c**, **d** Same as **a**, **b** but based on the 30–60-day filtered GPCP rainfall data

0.81, both exceeding the 99% confidence level. To quantitatively represent the interannual variation of these two leading patterns of BSISO intensity over the ASM region from 1981 to 2014, we define the standardized OLR-based PC1 (PC2) time series as the BIVI1 (BIVI2) (Fig. 2). The BIVI1 or BIVI2 magnitude actually indicates the anomalous state of BSISO intensity in the corresponding mode for each year. For instance, the BIVI1 value in 1996 was greater than 2, indicating significantly enhanced BSISO activity over the ASM region or very strong BSISO intensity. In contrast, the BIVI1 in 2010 was less than -1 , implying that the BSISO activity over the entire ASM area was suppressed significantly or the BSISO intensity was very weak. Table 1 lists the strong and weak years based on the BIVI1 and BIVI2, respectively. Note that the BIVI1 also shows an interdecadal fluctuation (Fig. 2a), with weak BSISO years predominating over the epochs from 1981 to 1995 and after 2010, while the strong years mostly occurring in the epoch 1996–2009. The mechanism for such an interdecadal BSISO fluctuation demands further investigation in the future.

4 Interannual variation of the first EOF mode of BSISO intensity

As shown in Fig. 1a, c, the first EOF mode of BSISO intensity exhibits a spatially coherent strengthening or weakening of BSISO activity over the SASM and EA/WNP region, indicating that the northward-propagating branches are interconnected by the equatorial eastward propagation from

the EIO to EWP. Therefore, the interannual variability of such a mode is explored in terms of these three propagating components.

4.1 The equatorial eastward propagation

The power spectra of the equatorial convection–circulation coupled system are concentrated within the 30–60-day period and zonal wavenumber one band during both strong and weak years (Fig. 3a, b). In strong years (Fig. 3a), the eastward propagating component within this frequency band is very strong, with the spectral power of OLR (850-hPa zonal wind) anomalies in the order of $9 \text{ W}^2 \text{ m}^{-4}$ ($0.15 \text{ m}^2 \text{ s}^{-2}$). The westward counterpart is relatively weak, with corresponding values of only $6 \text{ W}^2 \text{ m}^{-4}$ ($0.11 \text{ m}^2 \text{ s}^{-2}$), indicating that BSISO activities over the equatorial region are dominated by eastward propagation during strong years. In comparison, the strength of both the eastward and westward components within this frequency band is much weaker during weak years (Fig. 3b). The spectral power of OLR (850-hPa zonal wind) anomalies in the eastward direction is $6 \text{ W}^2 \text{ m}^{-4}$ ($0.05 \text{ m}^2 \text{ s}^{-2}$), and the corresponding value for the westward direction is $4 \text{ W}^2 \text{ m}^{-4}$ ($0.04 \text{ m}^2 \text{ s}^{-2}$). As the equatorial eastward-propagating signal is as weak as its westward-propagating counterpart, the dominant role of eastward propagation over the equatorial region becomes less obvious.

To further examine the difference of the equatorial eastward propagation, we compare the composite evolution of BSISO-related OLR and 850-hPa wind anomalies during phases 1–8 of BSISO cycles between strong and weak

Fig. 2 a Time series (solid line) of BSISO Interannual Variation Index1 (BIV1) for the period 1981–2014. The BIV1 is defined by the standardized PC1 time series through projecting the BSISO intensity matrix calculated from the 30–60-day filtered OLR anomalies onto the EOF1 mode shown in Fig. 1a. The black dash line at BIV1 equal to 0.8 (–0.8) shows the threshold used to classify strong (weak) BSISO years for the first EOF mode of BSISO intensity. Also shown is the standardized PC1 time series (histogram) of EOF1 mode derived from the 30–60-day filtered GPCP rainfall anomalies. **b** As in **a**, except for the time series of BIV2 defined by the standardized PC2 time series

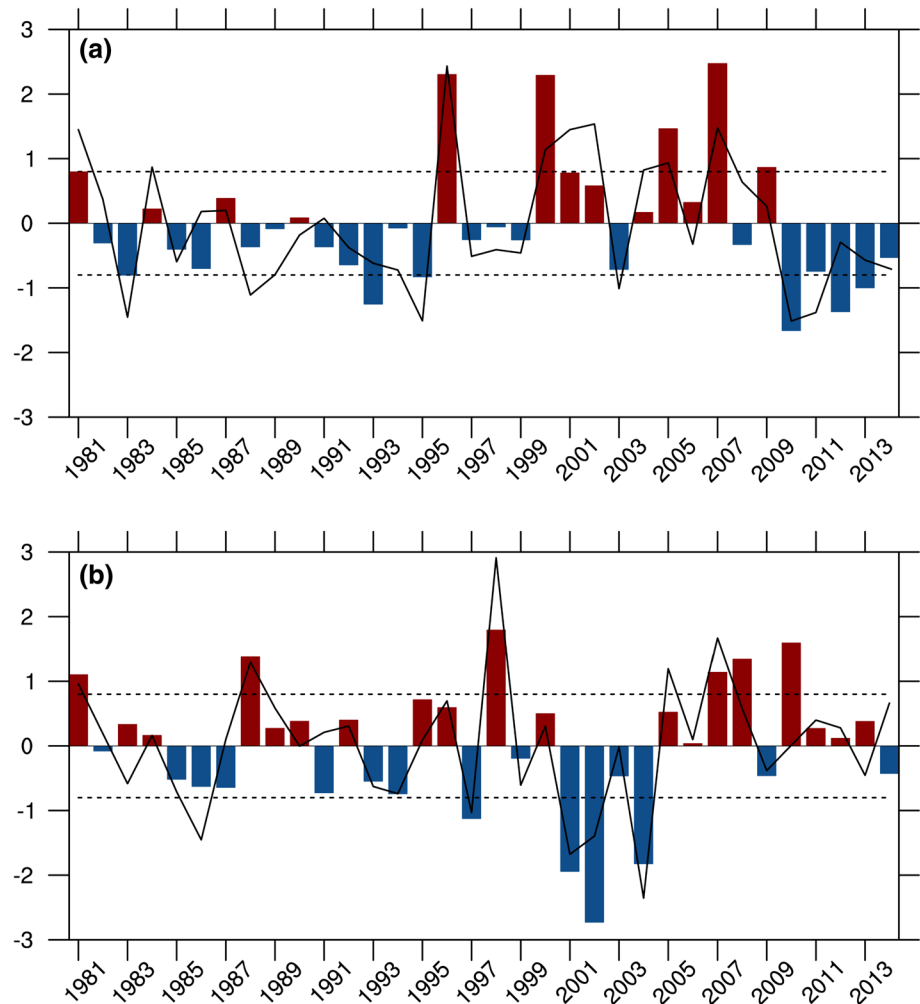


Table 1 Strong and weak BSISO years identified in the period 1981–2014

Mode	Type	List of years
Mode1	Strong years	1981, 1984, 1996, 2000, 2001, 2002, 2004, 2005, 2007
	Weak years	1983, 1988, 1995, 2003, 2010, 2011
Mode2	Strong years	1981, <i>1988, 1998, 2005, 2007</i>
	Weak years	1986, 1997, 2001, 2002, 2004

Strong (weak) BSISO years of the first EOF mode of BSISO intensity are defined as those with the BIV1 in Fig. 2a greater (less) than 0.8 (–0.8). Also listed are strong (weak) BSISO years of the second EOF mode of BSISO intensity defined based on the BIV2 in Fig. 2b with the criterion of 0.8. The years in which an El Niño (La Niña) develops during summer are shown in boldface (italic). See text for the definition of BIV1 and BIV2

years, based on the Quadruple Pattern Index (QPI) defined by Li and Mao (2016). During strong years (Fig. 4a), active convection anomalies originate from the EIO in phase 3, and significantly strengthen over the EEIO in phases 4–5. These well-developed active convection anomalies are

accompanied by strong zonal wind convergence at low levels, with anomalous westerlies (easterlies) to the west (east). This phase relationship between convection and zonal wind at low levels is consistent with the convectively coupled Kelvin–Rossby wave packet proposed by Wang and Xie (1997). Such a kind of coupled wave packet further lead to a zonal asymmetry in the planetary boundary layer (PBL; averaged between 925 and 1000 hPa) moisture field, with a positive (negative) specific humidity center being located to the east (west) of the convection center (not shown), thus forming an potentially unstable stratification ahead of the convection center (Hsu and Li 2012). Therefore, strong active convection continuously moves eastward across the Maritime Continent in phase 6 and reaches the EWP in phases 7–8.

During weak years (Fig. 4b), although the active convection anomalies initiated over the EIO in phase 3 are comparable with those during strong years, the following growth in phases 4–5 is weak. As a result, the active convection anomalies over the EEIO is much weaker, with no obvious zonal wind convergence accompanied, indicating that the convectively coupled Kelvin–Rossby wave packet

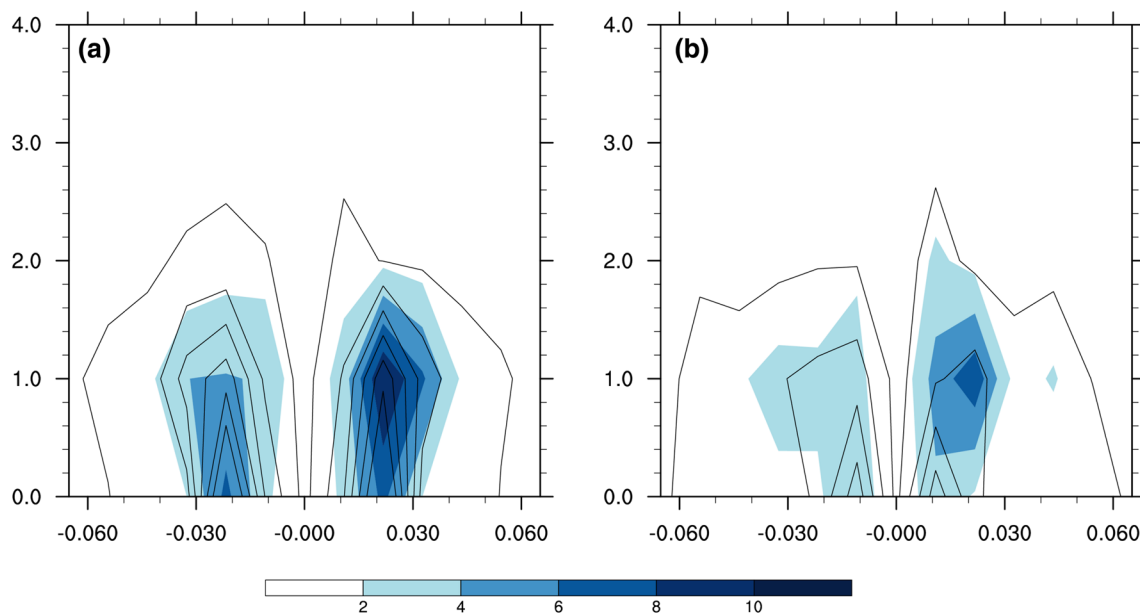


Fig. 3 Wavenumber–frequency power spectra of the anomalies of boreal summer (1 June to 31 August) equatorial (10°S–10°N) intraseasonal OLR (color scale, $W^2 m^{-4}$) and 850-hPa zonal wind (contours, $m^2 s^{-2}$, the contours start from 0.01 with an interval of 0.03) for a strong and **b** weak BSISO years of the first EOF mode of BSISO intensity

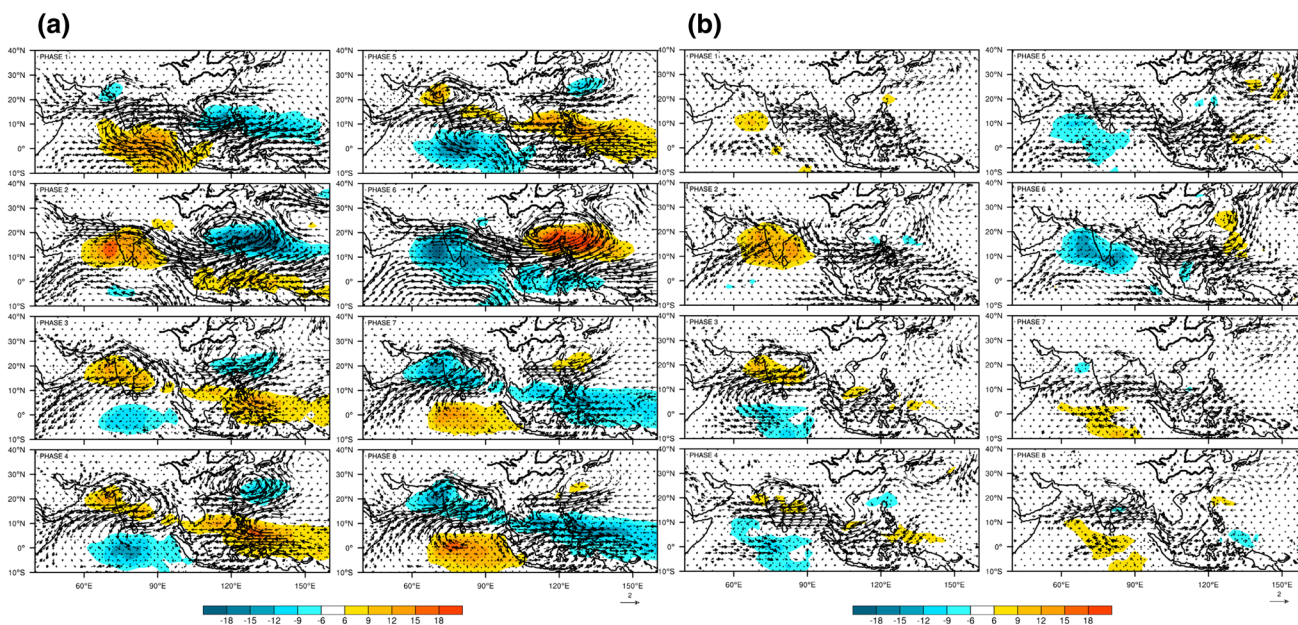


Fig. 4 Composite evolution of the 30–60-day filtered OLR (color scale, $W m^{-2}$) and 850-hPa wind (vectors, $m s^{-1}$) anomalies during a BSISO cycle for phases 1–8 in **a** strong and **b** weak BSISO years of the first EOF mode of BSISO intensity. Only shown are the OLR and

horizontal wind anomalies that are statistically significant at the 95% confidence level. The magnitude of the reference vector is provided at the bottom right

fails to develop. Consequently, the equatorial eastward-propagating signal over the EIO is very weak, with its PBL moisture nearly symmetric to the active convection center (not shown). The active convection anomalies then decay

dramatically around the Maritime Continent in phase 6, leading to very weak convection propagate into the EWP in phases 7–8. The above comparison suggests that the development of active convection anomalies over the

EEIO is critical to the formation of convectively coupled Kelvin–Rossby wave packet and the strength of equatorial eastward propagation.

To reveal why active convection anomalies develop significantly over the EEIO during strong years while not during weak years, we examine the differences of anomalous moisture and vertical motion in phases 3 (phases 7) between strong and weak years. As shown in Fig. 4, phase 3 (phase

7) is the phase prior to the development of active (inactive) convection over the EEIO. Because the circulation structure in phase 3 is opposite to that in phase 7, we only show the contrasts between strong and weak years for phase 3 in the following sections for the sake of brevity. During strong years (Fig. 5a), there is strong ascent over almost the entire troposphere between 60°E and 80°E, corresponding to the active convection initiated over the EIO (Fig. 4a). Note that

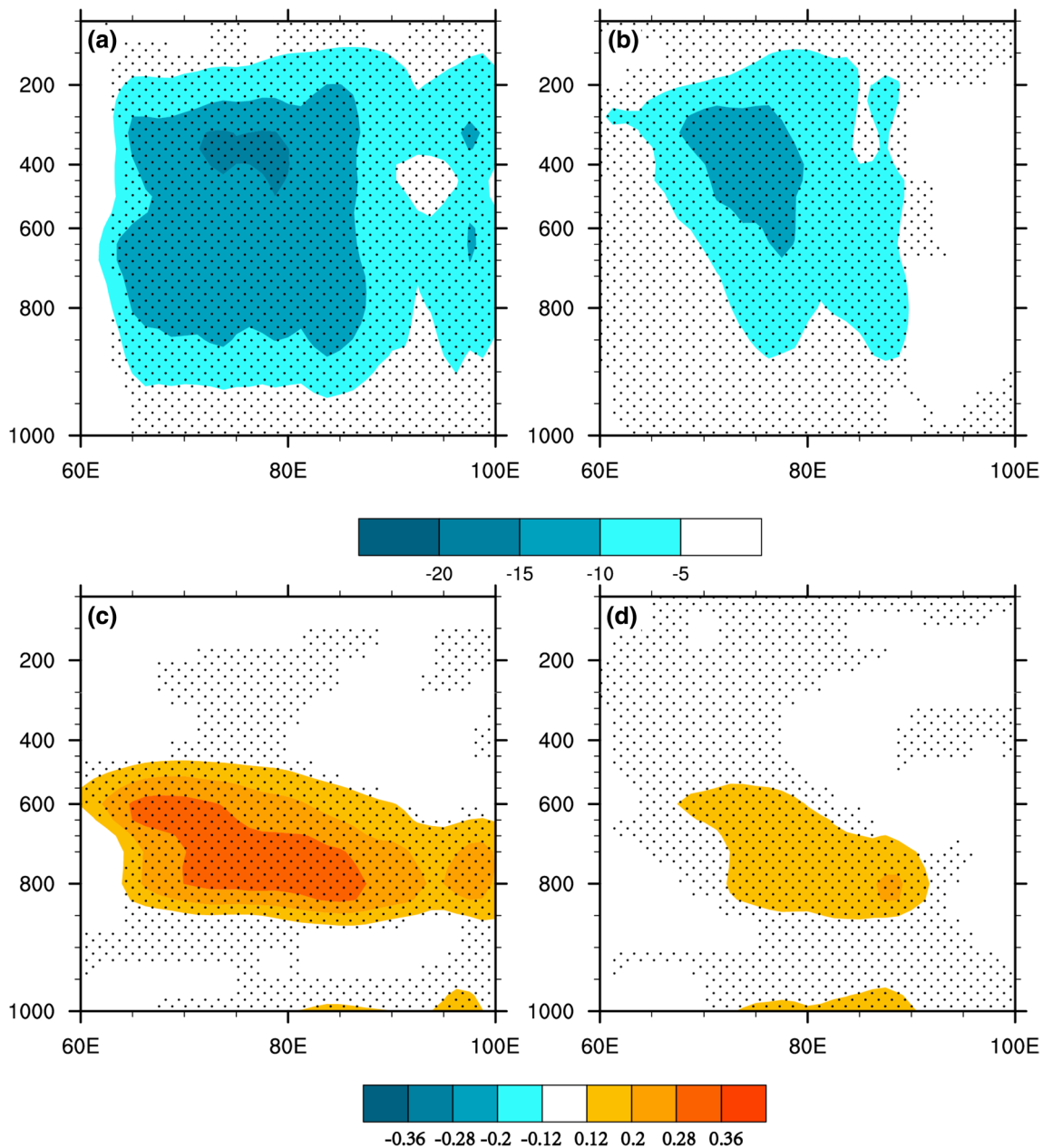


Fig. 5 Pressure–longitude cross sections of the equatorial (5°S–5°N) 30–60-day filtered vertical motion (color scale, $10^{-3} \text{ Pa s}^{-1}$) in the phase prior to the development of active convection anomalies over the EEIO (5°S–5°N, 90°–100°E), corresponding to phase 3 during the BSISO cycle shown in Fig. 4, for **a** strong and **b** weak BSISO

years of the first EOF mode of BSISO intensity. Stippling indicates the regions where vertical velocity anomalies are statistically significant at the 95% confidence level. **c, d** As in **a, b** except for the 30–60-day filtered specific humidity (color scale, g kg^{-1})

another strong ascent is observed over the longitude belt of 90°–100°E, providing a favorable dynamical condition for the development of active convection over the key EEIO. Meanwhile, within this key longitudinal zone, there are two positive moisture anomalies in the vertical (Fig. 5c), one in the near-surface layer (950–1000 hPa) and another in the middle troposphere (600–850 hPa). Such an anomalous vertical structure with moisture decreasing with height in the PBL, along with the strong ascending motion, indicate that an unstable PBL exists, thus leading to strong active convection develops over the key EEIO.

In contrast, only weak ascending motion less than $5 \times 10^{-3} \text{ Pa s}^{-1}$ is present in the mid-low troposphere (600–900 hPa) over the EEIO during weak years (Fig. 5b). Weak positive moisture anomalies in the middle troposphere are associated with this weak ascending motion. However, there are no significant positive moisture anomalies between 90°E and 100°E in the near-surface layer (Fig. 5d), indicating that the unstable PBL is absent. As a consequence, the development of active convection over the EEIO is weak in the following phases.

To further reveal the reason for the different vertical structures of moisture between strong and weak years, moisture budgets in phase 3 are analyzed according to Eq. (2) (Fig. 6). In strong years, moisture convergence and moisture vertical flux are the major terms in determining the

moisture tendency in the PBL (Fig. 6a–d). As the increasing tendency due to the moisture convergence term is larger than the decreasing tendency due to the moisture vertical flux term, the net effect of moisture vertical transport is to generate positive moisture anomalies in the PBL over the EEIO (Fig. 6b, c). Although the condensation latent heat term tends to decrease the moisture, its contribution is negligible in the PBL (Fig. 6d). The moisture horizontal advection term also makes a minor contribution, which is smaller by at least one order of magnitude than that from each of the other three terms (Fig. 6a). During weak years, in contrast, the moisture tendencies caused by moisture convergence and moisture vertical flux are much weaker (Fig. 6f, g), and almost cancel each other. The contributions of the condensation latent heat term and moisture horizontal advection term can also be negligible in the PBL (Fig. 6e, h). As a result, no significant moisture anomalies are observed between 90°E and 100°E (Fig. 5d).

Hsu and Li (2012) also emphasized the important role of PBL moisture convergence in the propagation of ISOs. They pointed out that the leading component in the moisture convergence term is the transport of seasonal-mean moisture by the intraseasonal ascending motion, which is associated with the BSISO-related wind convergence in the PBL, implying that multi-scale interaction is vital for ISO development. To identify the multi-scale interactive processes that determine

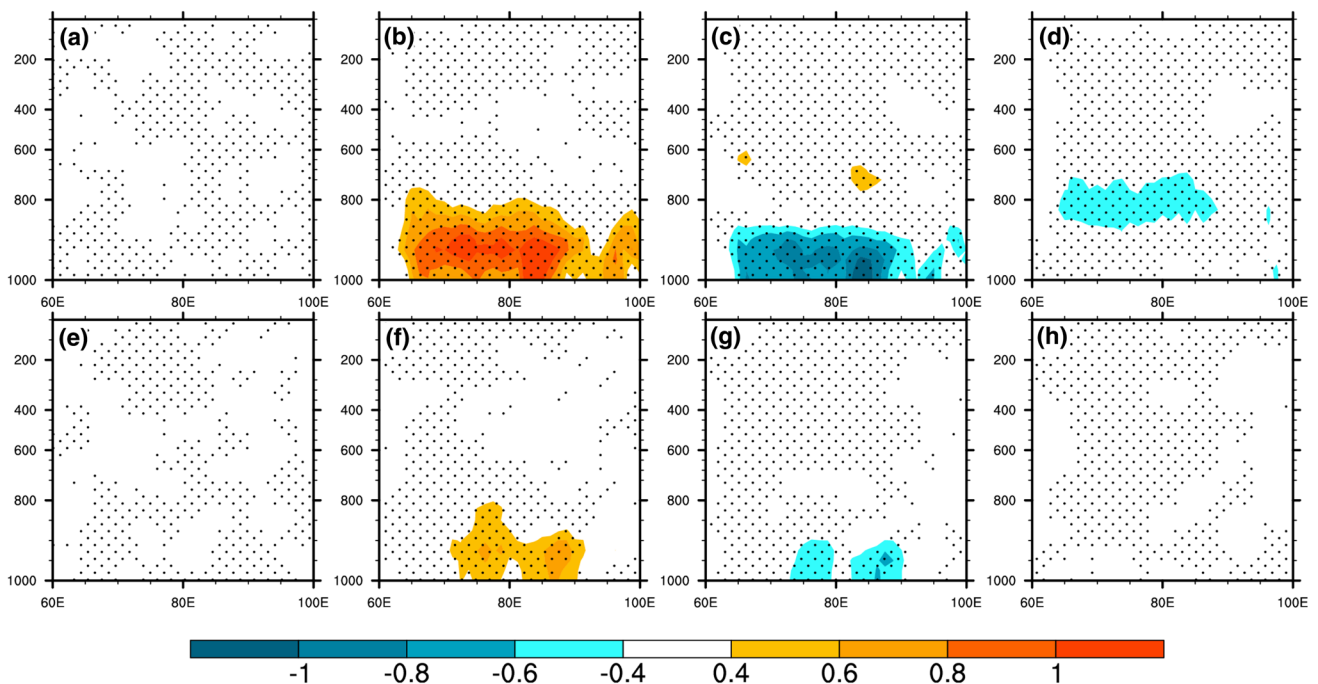


Fig. 6 Pressure–longitude cross sections of the equatorial (5°S–5°N) 30–60-day filtered moisture tendency (color scale, 10^{-8} g s^{-1}) at the same stage as in Fig. 5 due to **a** the horizontal moisture advection term, **b** the moisture convergence term, **c** the moisture vertical flux

term and **d** the latent heating term for strong BSISO years of the first EOF mode of BSISO intensity. Stippling indicates the regions where the moisture tendency is statistically significant at the 95% confidence level. **e–h** As in **a–d**, except for weak BSISO years

the strength of moisture convergence in the PBL over the EEIO, we decompose each variable in the moisture convergence term into three components: the low-frequency background component (with period longer than 120 days, denoted by an overbar), the BSISO-related component (with period of 30–60 days, denoted by a prime) and the high-frequency component (with period shorter than 30 days, denoted by a double prime). Therefore, the BSISO-related moisture convergence can be decomposed into nine terms as in the following equation (Hsu and Li 2012), with the multi-scale interactive terms labeled in Eq. (3) with letters A to I.

$$\begin{aligned}
 (q\nabla \cdot \vec{V})' &= (\bar{q}\nabla \cdot \bar{\vec{V}})'_A + (\bar{q}\nabla \cdot \vec{V}')'_B + (\bar{q}\nabla \cdot \vec{V}'')'_C + (q'\nabla \cdot \bar{\vec{V}})'_D \\
 &+ (q'\nabla \cdot \vec{V}')'_E + (q''\nabla \cdot \vec{V}'')'_F + (q''\nabla \cdot \bar{\vec{V}})'_G \\
 &+ (q''\nabla \cdot \vec{V}')'_H + (q''\nabla \cdot \vec{V}'')'_I. \tag{3}
 \end{aligned}$$

The relative contributions of terms A–I are shown in Fig. 7. The positive moisture anomalies in the PBL over the EEIO come mainly from the convergence of seasonal-mean moisture by the BSISO-associated flows in the PBL (term

B: $\bar{q}\nabla \cdot \vec{V}'$) during both strong and weak years. Therefore, the development of active convection associated with BSISO over the EEIO is determined by the multi-scale interaction of two factors: the BSISO-related wind convergence and the seasonal-mean moisture in the PBL.

During strong years, the seasonal-mean SSTs over the central–eastern North Pacific (CNP) are much higher than those during weak years, with the largest SST differences in excess of 0.8 K (Fig. 8a). In response to the warmer SSTAs over the CNP along with negative SSTAs over the SCS, anomalous low-level westerlies are induced over the tropical Pacific from western Pacific towards the CNP (Fig. 8a, b). Note that the SST cooling is also present over western North Pacific (Fig. 8a), in contrast with the robust CNP warming to force an anomalous cyclonic circulation (Fig. 8a, b), weakening the western North Pacific high. Meanwhile, significant negative SSTAs are observed over the tropical Indian Ocean west of 80°E (Fig. 8a), which forms a zonal interoceanic SSTA contrast with the positive SSTA over the CNP. As a response to this interoceanic SSTA gradient, anomalous westerlies are also induced over the tropical Indian Ocean (Fig. 8a, b), and connect

Fig. 7 Multi-scale interactive terms (indicated by letters A–I) contributing to the 30–60-day filtered moisture convergence ($10^{-8} \text{ g (g s)}^{-1}$) in the PBL (averaged between 925 and 1000 hPa) at the same stage as in Fig. 5 for **a** strong and **b** weak BSISO years of the first EOF mode of BSISO intensity. Also shown is the sum of the nine terms. See text for details of each term

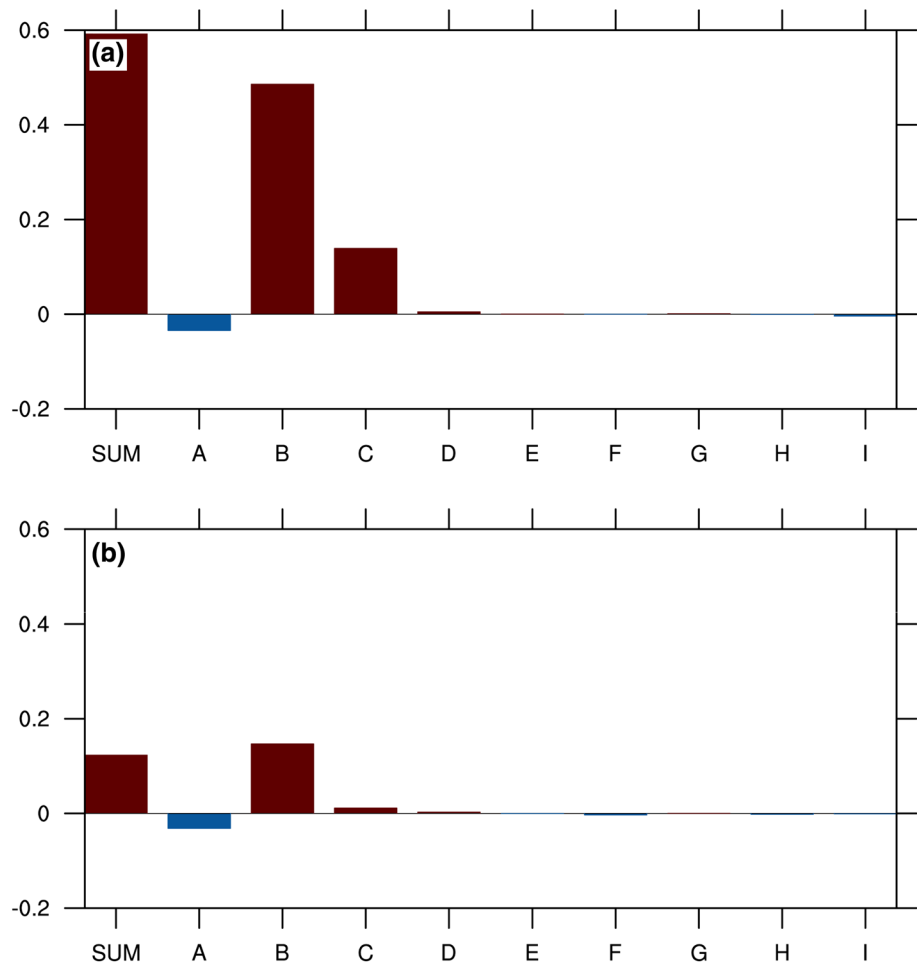
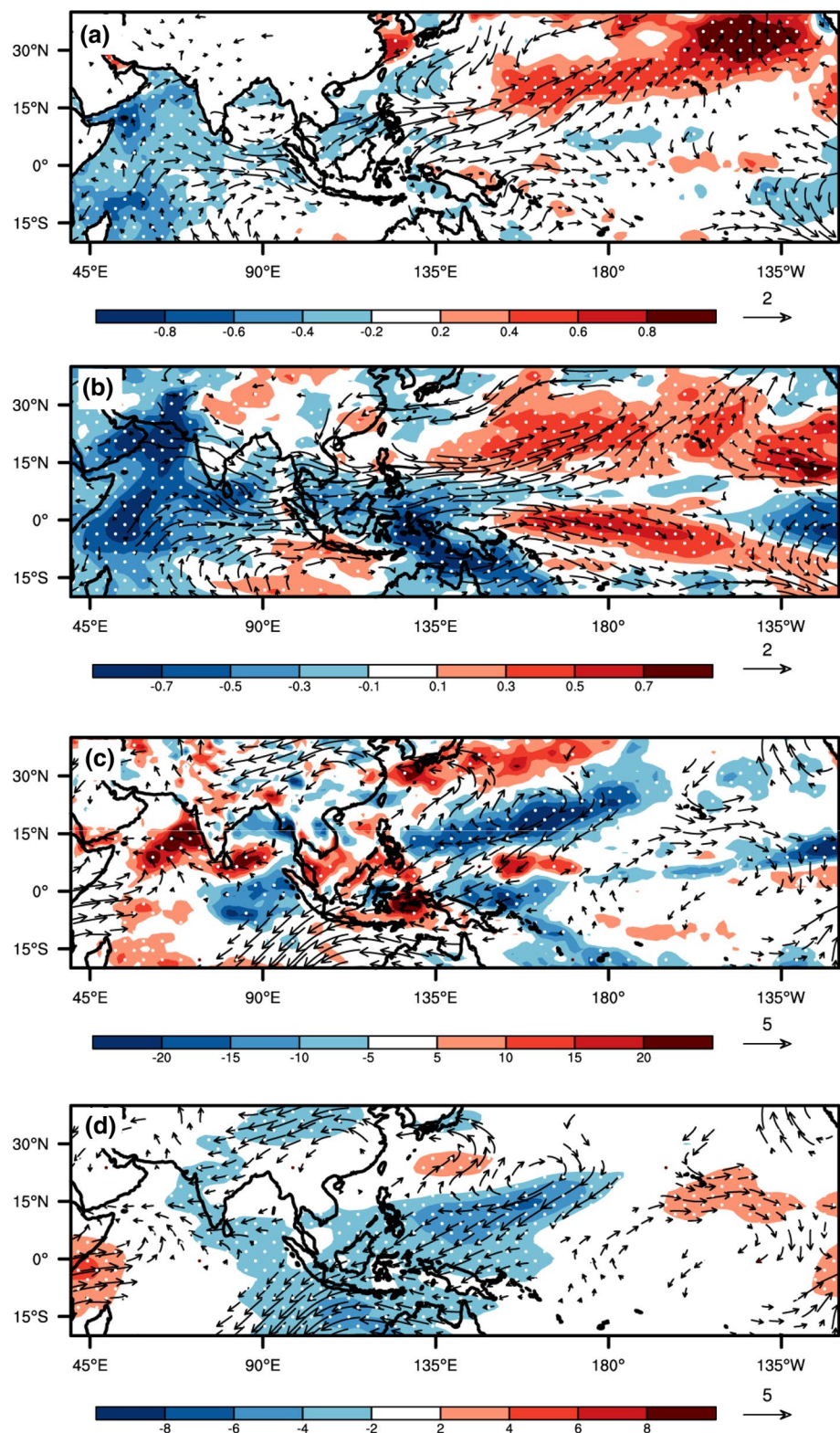


Fig. 8 Differences between strong and weak BSISO years of the first EOF mode of BSISO intensity, in terms of boreal summer seasonal-mean **a** SST (color scale, K) and PBL winds (vectors, m s^{-1}), **b** specific humidity (color scale, g kg^{-1}) in the lower atmosphere (averaged between 700 and 850 hPa) and 850-hPa winds (vectors, m s^{-1}), **c** 500-hPa vertical motion (color scale, $10^{-3} \text{ Pa s}^{-1}$) and 200-hPa winds (vectors, m s^{-1}), and **d** easterly vertical shear defined as the difference of zonal wind between 200 and 850-hPa (color scale, m s^{-1}) and 200-hPa winds (vectors, m s^{-1}). Stippling indicates the regions where the differences of key variables are statistically significant at the 90% confidence level. Vector is displayed only when its zonal or meridional component is statistically significant at the 90% confidence level



together with the downstream westerlies over the CNP. It is thus obvious that the significant positive SSTAs over the CNP along with negative SSTAs the tropical Indian Ocean play a key role in strong BSISO years.

Note that the anomalous westerlies in the PBL deflect southward when encountering Sumatra Islands due to the blocking and frictional effect of topography, forming an anomalous cyclonic circulation south of the equator (Fig. 8a).

The similar cyclonic circulation also exists at 850 hPa (Fig. 8b). Such an anomalous cyclonic circulation in the lower atmosphere tends to bring about the moisture to converge, thus producing an positive moisture anomaly over EEIO (Fig. 8b). Furthermore, the convergence of anomalous horizontal winds in the lower troposphere also leads to anomalous ascending motions (Fig. 8c), which transport more moisture upward from sea surface to the tropospheric atmosphere (not shown), again contributing to the wetter background over the EEIO (Fig. 8b). As a consequence, the local moist static energy is increased (not shown), providing a favorable background for stronger intraseasonal convection over the EEIO. The seasonal-mean–intraseasonal interaction between the wetter background and intraseasonal wind convergence ($\bar{q}\nabla \cdot \bar{V}'$) leads to positive moisture anomaly in the PBL over the EEIO in phase 3 (Fig. 5c), which is conducive to strong BSISO-related active convection developing and subsequently propagating eastward. Contrarily, in weak BSISO years, the reversed SSTA contrast between the cooler CNP and the warmer tropical Indian Ocean leads to insignificant enhancement of active convection anomalies over the EEIO and the resultant equatorial eastward propagation is thus weak.

4.2 The northward propagation over the SASM region

During strong years (Fig. 9a), the largest spectral component of both OLR and 850-hPa zonal wind anomalies is concentrated within the 25–100-day period, wavenumber one band in the northward-propagating direction, with the spectral power of OLR (850-hPa zonal wind) anomalies being $13 \text{ W}^2 \text{ m}^{-4}$ ($0.28 \text{ m}^2 \text{ s}^{-2}$). By contrast, the strength of the northward propagating component within the same frequency band is much weaker during weak years (Fig. 9b), with the spectral power of OLR (850-hPa zonal wind) anomalies being only $5 \text{ W}^2 \text{ m}^{-4}$ ($0.1 \text{ m}^2 \text{ s}^{-2}$). The latitude–lag-time diagrams show that anomalous signals of both OLR and 850-hPa zonal wind clearly propagate northward along the Indian longitudes during strong years (Fig. 9c), while the anomalous OLR and the accompanying 850-hPa zonal wind become very weak north of 15°N during weak years (Fig. 9d).

To find out what mechanism is responsible for the interannual variation of northward propagation over the SASM region, we compare the meridional-vertical cross sections of the BSISO-related key variables (vertical motion, specific humidity, vorticity and divergence) in the northward propagation of active convection (phases 5–7) between strong and weak years (Fig. 10). During strong years, strong ascending motion through the troposphere is seen to coincide with the convection center (Fig. 10a), which results from anomalous convergence in the low-levels and strong anomalous divergence aloft (Fig. 10c). Note that the convergence in the PBL exhibits an obvious meridional asymmetry, with the

convergence covering about 6 (3.75) latitudes north (south) of the central convection. The PBL convergence ahead of convection center favors new convection to generate, thus leading to the northward propagation of BSISO. According to Jiang et al. (2004) and Bellon and Sobel (2008), the PBL convergence ahead of the convection center is actually caused by the barotropic cyclonic vorticity in the free atmosphere (Fig. 10d), which in turn comes from the easterly vertical shear mechanism (Jiang et al. 2004) and the advection of anomalous baroclinic vorticity by the seasonal-mean meridional baroclinic flow (Bellon and Sobel 2008). Note that the moisture in the middle and low levels shows a southward-tilted vertical structure, with the center of positive moisture anomalies located north of the convection center (Fig. 10b). Jiang et al. (2004) pointed out that this southward-tilted moisture vertical structure comes from moisture convection feedback mechanisms, which destabilizes the atmosphere ahead of the original convection center, thus leading to the northward propagation.

In weak years, the weaker northward-propagating convection is accompanied by weaker ascending motions through the troposphere (Fig. 10e). Although the asymmetry of vorticity can still be discerned, the cyclonic vorticity north of the convection center is only around $1.5 \times 10^{-6} \text{ s}^{-1}$ (Fig. 10h), with the induced PBL convergence nearly symmetric with respect to the convection center (Fig. 10g). The positive moisture anomalies associated with the northward-propagation BSISO are also much weaker and show little meridional asymmetry in the mid-low levels (Fig. 10f). The weak meridional asymmetry of both PBL convergence and low-level moisture indicates that the weaker northward propagation over the SASM area in weak years might be the combined outcome of easterly vertical shear, vorticity advection and moisture mechanisms.

Note that the easterly vertical shear, vorticity advection and moisture-convection feedback mechanisms are all physically interpreted as the seasonal-mean–BSISO interaction. To further determine the key seasonal-mean–BSISO interactive processes responsible for the interannual variations of northward propagation over the SASM region, we examine the changes of seasonal-mean easterly vertical shear (defined as the difference of zonal wind between 200- and 850-hPa), vertical northerly shear (defined as the difference of meridional wind between 200- and 850-hPa), meridional wind in the PBL (defined as the meridional wind averaged between 1000- and 925-hPa), meridional gradient of low-level (700–850 hPa) specific humidity and the associated intraseasonal variations. As shown in Fig. 8b, the anomalous low-level westerlies are enhanced over the Indian Subcontinent–Bay of Bengal in response to the SSTA contrast between the tropical Indian Ocean and CNP, which tend to strengthen the locally easterly vertical shear significantly during strong years

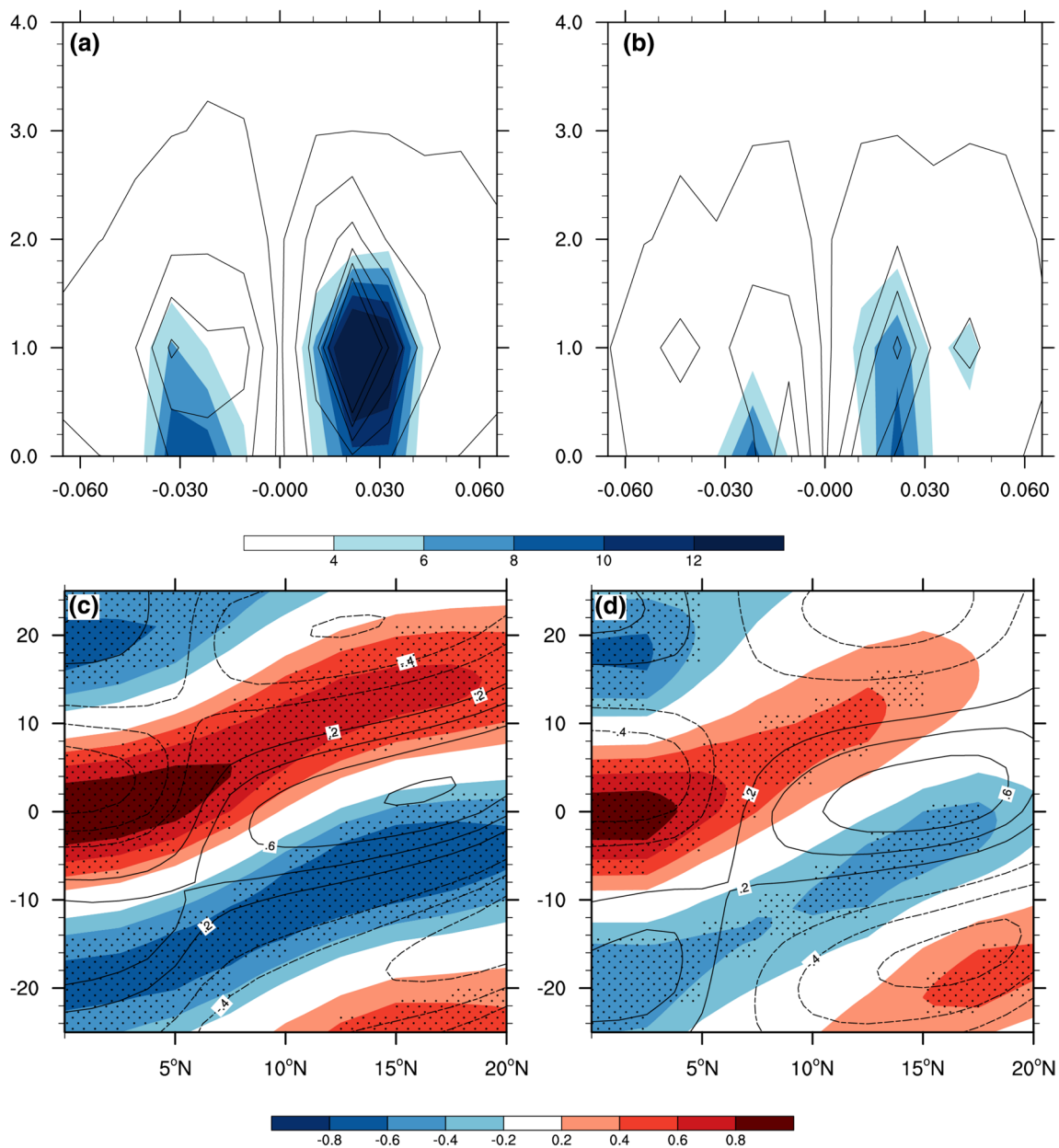


Fig. 9 Finite domain wavenumber–frequency power spectra of the anomalies of boreal summer intraseasonal OLR (color scale, $W^2 m^{-4}$) and 850-hPa zonal wind (contours, $m^2 s^{-2}$, the contours start from 0.01 with an interval of 0.05) calculated over the SASM area ($10^{\circ}S-30^{\circ}N, 60^{\circ}-100^{\circ}E$) for **a** strong and **b** weak BSISO years of the first EOF mode of BSISO intensity. Also shown are latitude–lag-time diagrams of correlation coefficients of the 30–60-day filtered OLR (color scale) and 850-hPa zonal wind (contours) anomalies over the

Indian Ocean longitudes ($60^{\circ}-100^{\circ}E$) with respect to the area-averaged 30–60-day filtered OLR anomaly over the EIO ($5^{\circ}S-5^{\circ}N, 60^{\circ}-100^{\circ}E$) for **c** strong and **d** weak BSISO years of the first EOF mode of BSISO intensity. The contour interval is 0.2, with the zero contour omitted and negative contours dashed. Stippling indicates the regions where correlation coefficients of OLR anomalies are statistically significant at the 95% confidence level

(Fig. 8d). On the other hand, the negative SSTAs over the tropical Indian Ocean (Fig. 8a) may also enhance the land–sea thermal contrast, with the meridional temperature gradient increasing in tropospheric atmosphere (not shown), thus the easterly vertical shear is further intensified over the western Indian Subcontinent due to thermal

wind relation (Fig. 8d). In turn, such intensified easterly vertical shear enhances the northward propagation over the SASM sector through easterly vertical shear mechanism. Contrarily, the decreased easterly vertical shear weaken the northward propagation off the equator during weak years.

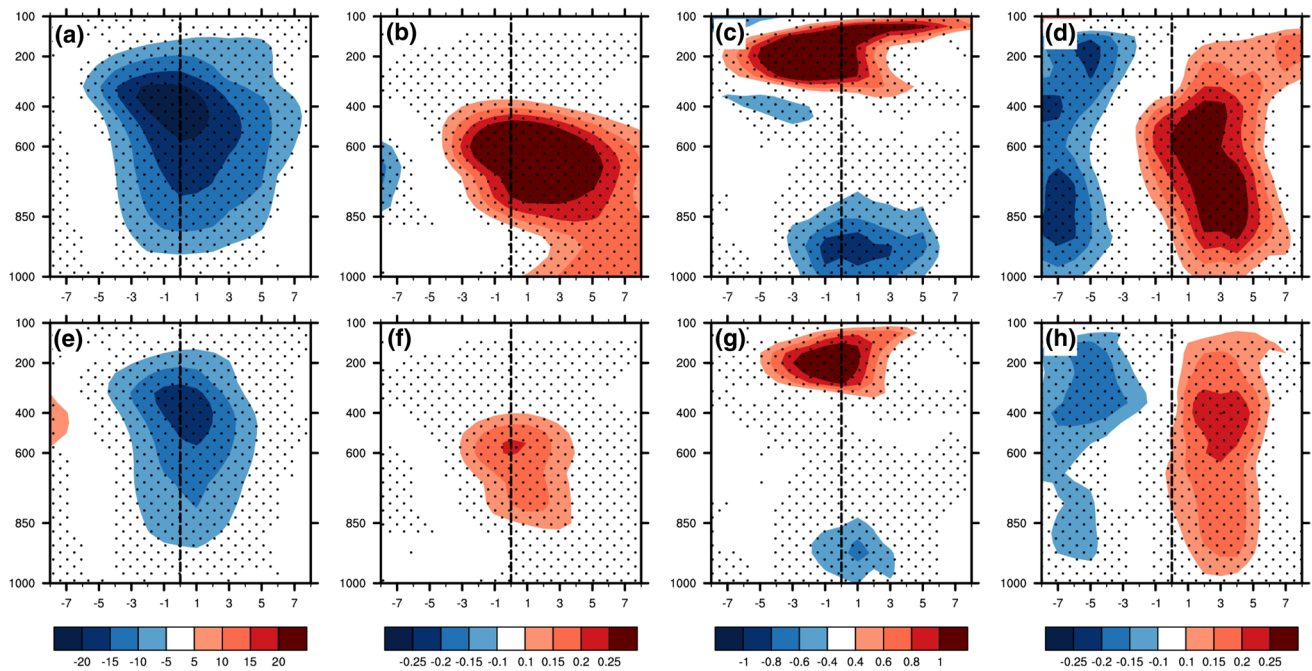


Fig. 10 Meridional-vertical cross section of anomalous **a** vertical motion (color scale, $10^{-3} \text{ Pa s}^{-1}$), **b** specific humidity (color scale, g kg^{-1}), **c** divergence (color scale, 10^{-6} s^{-1}) and **d** vorticity (color scale, 10^{-5} s^{-1}) during the northward propagation of active convection along the Indian longitudes (60° – 100°E) in phases 5–7 of a BSISO cycle during strong BSISO years of the first EOF mode of BSISO

Note from Fig. 8a that there is no significant difference in the PBL meridional wind between strong and weak years over the EIO, and meridional gradient of the low-level specific humidity even decrease over the EIO during strong years (Fig. 8b), suggesting that the seasonal-mean moisture backgrounds are not dominant factors in the moisture mechanism to cause the interannual variation of northward propagation over the equatorial area. On the other hand, during strong (weak) years, the intensified (weakened) equatorial BSISO signals are certainly accompanied by enhanced (weakened) upward motions, which bring more (less) moisture upward, thus strengthening (weakening) the low-level moisture anomalies in association with the active BSISO. The seasonal-mean southerlies in the PBL further shift the strong (weak) low-level specific humidity center to the north (Fig. 10b), leading to a strong (weak) meridional asymmetry of low-level moisture, thus contributing to a stronger (weaker) northward propagation over the EIO.

4.3 The northward propagation over the EA/WNP region

The meridional wavenumber–frequency power spectrum analysis shows that the BSISO over the EA/WNP region has both northward and southward propagating components

concentrating within a band of 25–100 days and meridional wavenumbers 1–2 (Fig. 11). During strong years, the northward propagating signal for both anomalous OLR ($14 \text{ W}^2 \text{ m}^{-4}$) and 850-hPa zonal wind ($0.33 \text{ m}^2 \text{ s}^{-2}$) is much stronger than that of the southward propagating components (the corresponding values are $5 \text{ W}^2 \text{ m}^{-4}$ and $0.15 \text{ m}^2 \text{ s}^{-2}$) (Fig. 11a), indicating that the BSISO over the EA/WNP region is dominated by the northward propagating component. In contrast, during weak years, the spectral power of OLR and 850-hPa zonal wind anomalies within the same band is much smaller (Fig. 11b). The latitude–lag-time diagrams show that strong signals of anomalous OLR and 850-hPa zonal wind propagate northward coherently from the EWP to WNP during strong years (Fig. 11c), while the northward propagating signals are much weaker and confined to south of 10°N during weak years (Fig. 11d).

To further figure out what is the major mechanism responsible for the interannual variation of northward propagation along the EA/WNP longitudes, the associated seasonal-mean backgrounds and intraseasonal anomalies are also compared. As mentioned above, during strong years, an anomalous east–west oriented vertical circulation is induced in response to the SSTA contrast between the warmer CNP and cooler SCS, with anomalous descending motion over the SCS, ascending motion over the tropical western–central Pacific

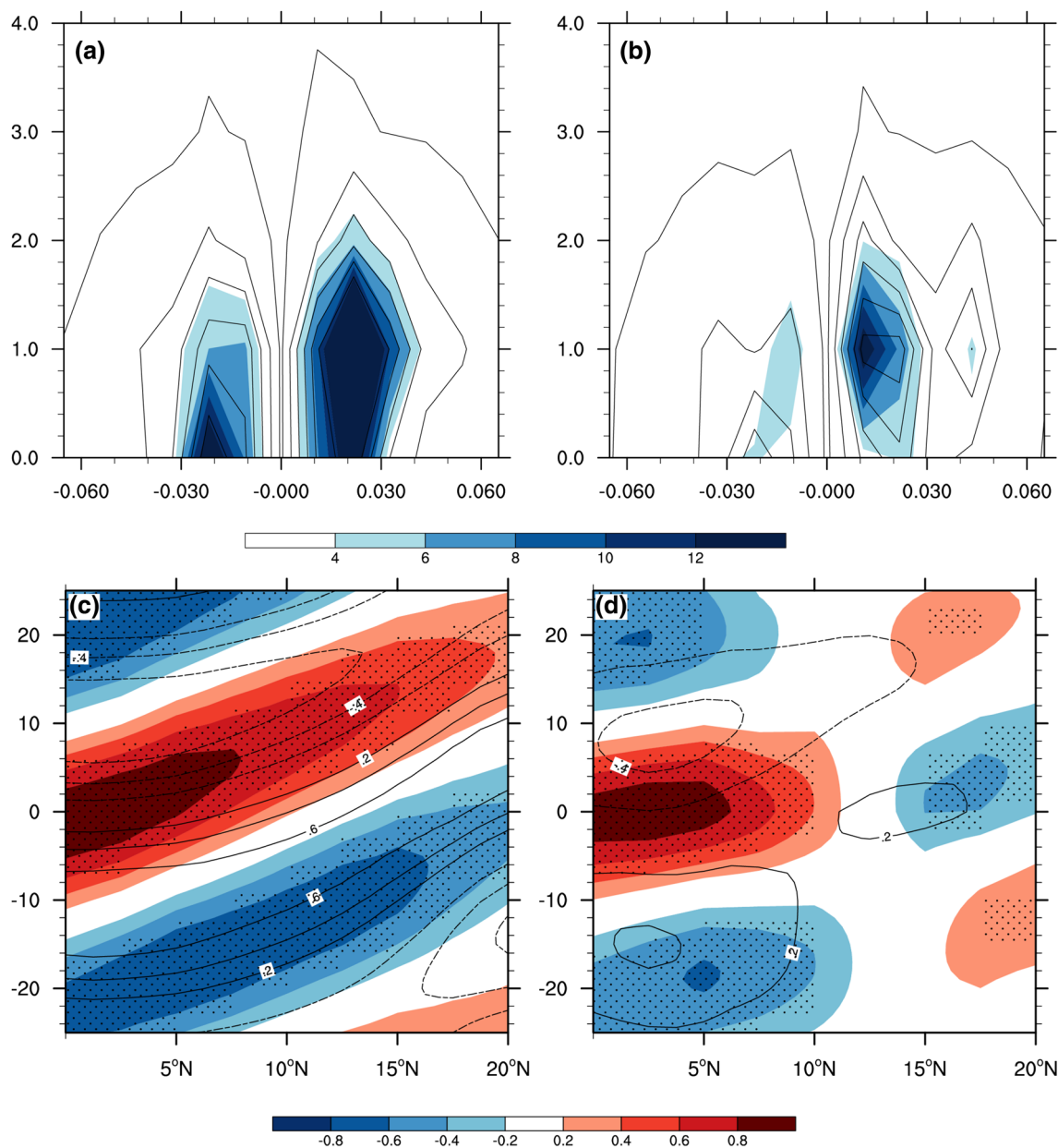


Fig. 11 **a, b** As in Fig. 9a, b except for wavenumber–frequency power spectra over the EA/WNP area (10°S–30°N, 110°–140°E). **c, d** As in Fig. 9c, d except for northward propagation along the EA/WNP lon-

gitudes (110°–140°E), taking the reference time series as the area-averaged 30–60-day filtered OLR anomaly over the EWP (5°S–5°N, 110°–140°E)

(Fig. 8c), and significant anomalous easterlies over the tropical western Pacific in the upper troposphere (Fig. 8d). Also observed is SST cooling over western North Pacific (Fig. 8a), which forms a SSTA contrast with the robust CNP warming to induce an anomalous cyclonic circulation over the western North Pacific, leading to anomalous westerlies over the tropical western Pacific in the lower troposphere (Fig. 8b). Therefore, the seasonal-mean easterly vertical shear over the tropical western Pacific increases significantly, leading to striking meridional asymmetries of vorticity and PBL convergence

with respect to the active convection center in association with the northward-propagating BSISO (Fig. 12c, d), thus intensifying the northward propagation. Note from Fig. 8b that the weakened meridional gradient of low-level moisture over the southern SCS is associated with the negative SSTA over the SCS (Fig. 8a). Meanwhile, the PBL southerlies become weaker east of the SCS. Both these seasonal-mean backgrounds tend to reduce the meridional asymmetry of moisture during strong years. Therefore, the obvious meridional asymmetry of middle and lower tropospheric moisture

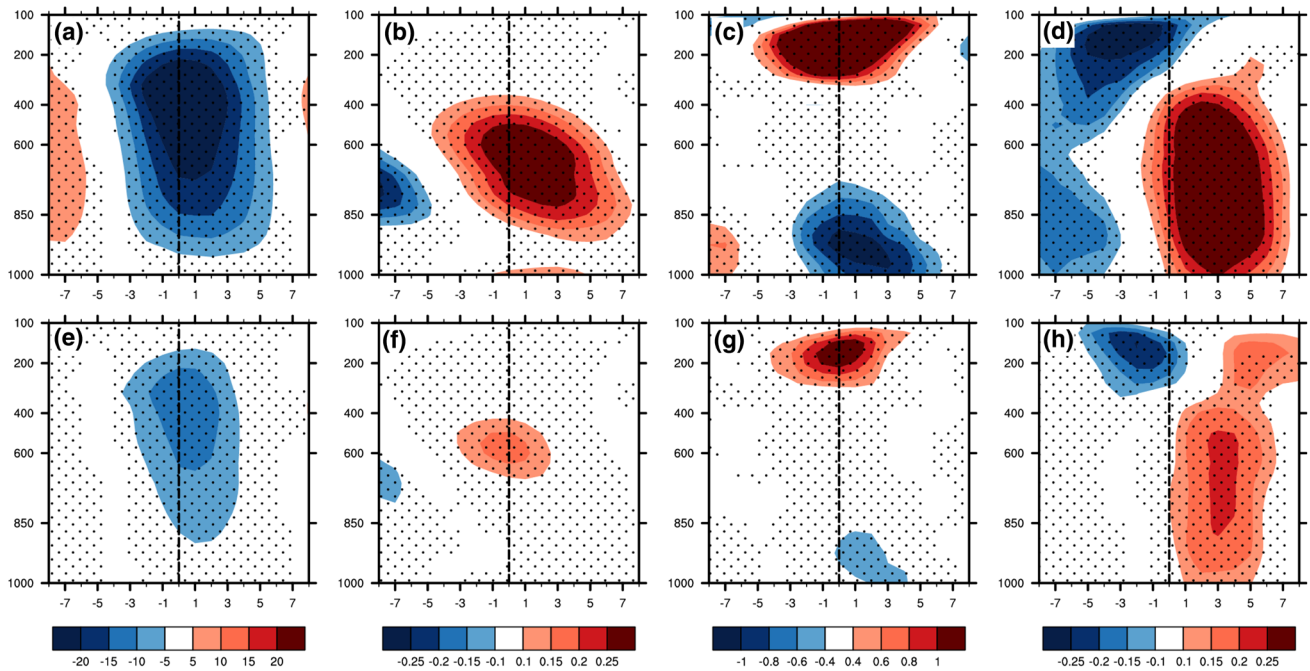


Fig. 12 As in Fig. 10 except for the situations of northward propagation along the EA/WNP longitudes (110° – 140° E) in phases 1–3 of a BSISO cycle

in the northward-propagating BSISO over this area (Fig. 12b) could only be attributed to the enhanced equatorial signals of BSISO activity through moisture mechanism, which is similar to the situation over the SASM region. Contrarily, the opposite-signed SSTAs over the SCS and CNP together with the weaker equatorial BSISO activity lead to weaker northward propagation over the EA/WNP region during weak years, characterized by weak meridional asymmetry of the middle and lower tropospheric moisture and vorticity as well as PBL convergence (Fig. 12f–h).

5 Interannual variability of the second EOF mode of BSISO intensity

The second EOF mode of BSISO activity, as shown in Fig. 1b, d, represents such a dipole pattern in intensity, with anomalously strong (weak) BSISO years referring to the ones with enhanced (weakened) BSISO activity over southeastern EIO while weakened (enhanced) activity over the EWP according to BIVI2 (Table 1). To examine whether the difference of the spatial distribution is connected with the propagation patterns, we also compare the composite evolution of BSISO-related OLR and 850-hPa wind anomalies between strong and weak years of the second EOF mode (Fig. 13). In strong years (Fig. 13a), active convection anomalies initiate from the EIO in phase 3, and strengthen significantly in phases 4–5. Although such active convection

anomalies tend to migrate both northward towards the Indian Subcontinent and eastward towards the Maritime Continent in phase 6, the convection signals have not developed strongly around the EWP in phases 7–8 and isolate with the upstream signals over SASM region.

In contrast, weaker active convection anomalies initiate over the EIO in phase 3 during weak years (Fig. 13b). These active convection anomalies slightly develop in phases 4–5, with negative OLR anomalies only around 10 W m^{-2} observed over the EIO. When active OLR anomalies occur over the Indian Subcontinent and northeastern Arabian Sea in phase 6, there is also active convection anomalies moving across the Maritime Continent, but the magnitude is $2\text{--}3 \text{ W m}^{-2}$ smaller compared with the strong years. However, strong active convection anomalies unexpectedly appear over the EWP in phases 7–8.

To understand why the strong BSISO activity is mostly confined to west (east) of the Maritime Continent (around 135° E) in strong (weak) years, we compare the associated seasonal-mean background between strong and weak years (Fig. 14). Significant negative SSTAs are observed over the equatorial eastern–central Pacific, while positive SSTAs are present over the tropical western Pacific and western Arabian Sea (Fig. 14a), showing a La Niña-like SSTA pattern. The atmospheric response to such a SSTA distribution is that anomalous ascending motion occurs between 90° E and 135° E, with strong descending motion to the east (Fig. 14c), indicating a strong Walker Circulation during strong years. Note that

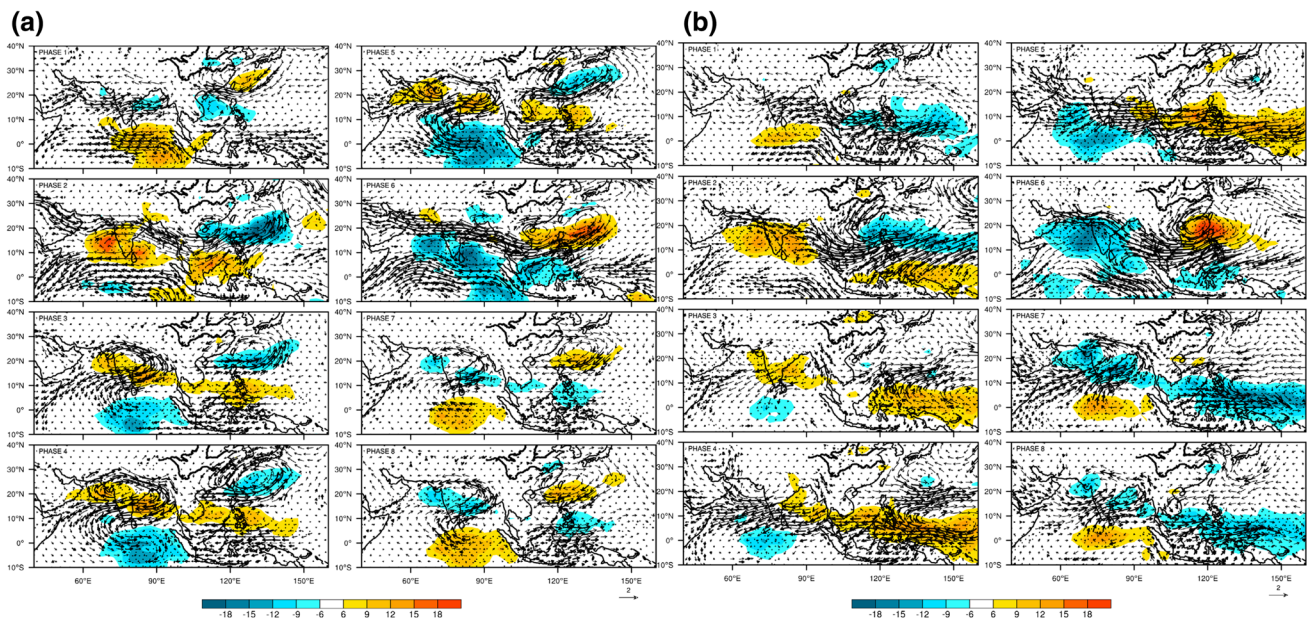


Fig. 13 As in Fig. 4 except for the situations in **a** strong and **b** weak BSISO years of the second EOF mode of BSISO intensity

the ascending branch is forced by strong convergence of the low-level easterlies from the cooler equatorial eastern–central Pacific (Fig. 14b). The zonal wind convergence further leads to strong moisture convergence (not shown), significantly moistening the lower tropospheric atmosphere over the southeastern EIO and Maritime Continent (Fig. 14b), and thus accumulating more moist static energy (Fig. 15). This background is favorable for intraseasonal convection to occur, leading to strong BSISO activity forming over the southeastern EIO (Fig. 13a). Meanwhile, the EWP east of 135°E is dominated by anomalous descents and low-level divergence (Fig. 14b, c), with the local moist static energy being reduced (Fig. 15). Such a background certainly inhibits the intraseasonal convection to develop, thus the upstream signals are difficult to grow sequentially east of the Maritime Continent (Fig. 13a). As a result, the intensity of BSISO activity over the EWP east of 135°E is reduced while that west of 135°E is enhanced, forming a dipole pattern (Fig. 1b, d). Conversely, the circulation background associated with the El Niño-like SSTA pattern mostly enhances the BSISO activity over the eastern EWP while restrains the activity over the southeastern EIO, generating the opposite dipole pattern.

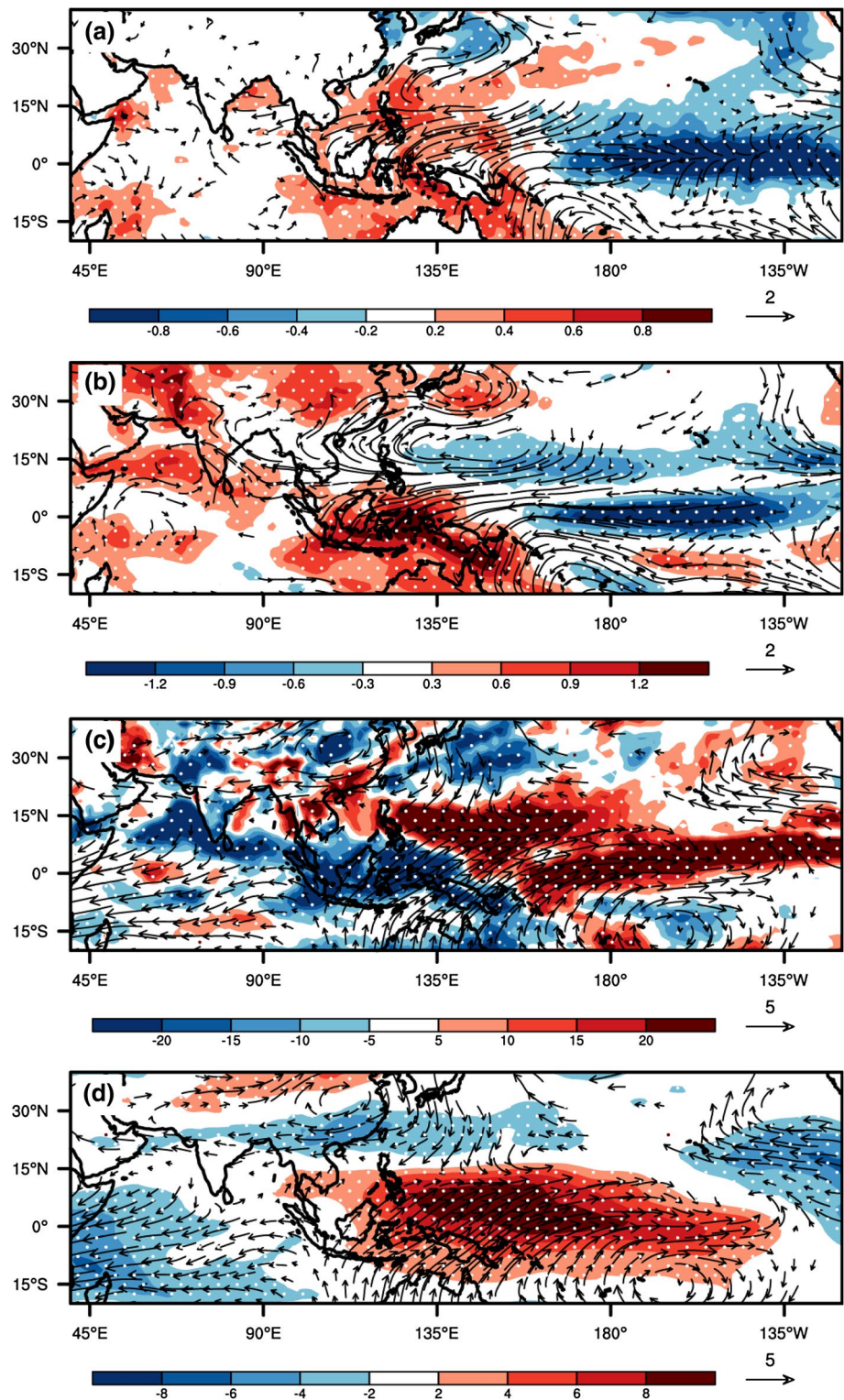
6 Different external forcing for interannual variations of two leading EOF modes of BSISO intensity

Composite analyses in Sects. 4 and 5 reveal that the interannual variations of the two leading EOF modes of BSISO activity are both associated with the corresponding

seasonal-mean external forcing. The first EOF mode is strongly influenced by the summer-mean SSTA contrast between the tropical Indian Ocean and CNP (Fig. 8a), with the warmer (cooler) CNP and cooler (warmer) tropical Indian Ocean inducing significant low-level westerly (easterly) anomalies over the tropical Indian Ocean to CNP during strong (weak) years. On the one hand, the anomalous westerlies (easterlies) over the EIO favor the development of strong (weak) equatorial BSISO activity over the EEIO, leading to strong (weak) equatorial eastward propagation. On the other hand, the easterly vertical shear over the western Indian Subcontinent and the tropical western Pacific are enhanced significantly, giving rise to strong (weak) northward propagation over the SASM and EA/WNP areas, respectively. Meanwhile, anomalous ascents (descents) dominate the equatorial areas from 60°E to 160°E (Fig. 16a), providing a coherently favorable (unfavorable) dynamical background for strong (weak) BSISO over the EIO to further propagate into the EWP. The BSISO activity over the EA/WNP region is thus connected together with the counterpart over the SASM region (Fig. 4), forming the spatially coherent strengthening (weakening) of BSISO activity over the entire ASM region.

In contrast, the second EOF mode is closely linked with ENSO-related SSTA pattern (Fig. 14a), with 80% of strong years being categorized as La Niña developing summers while 80% of the weak years as El Niño developing summers (Table 1). In association with the developing phase of La Niña (El Niño), an anomalously zonal–vertical circulation is observed along the equator during strong (weak) years (Fig. 16b), with anomalous ascents (descents)

Fig. 14 As in Fig. 8 except for differences between strong and weak BSISO years of the second EOF mode of BSISO intensity



accompanied by zonal wind convergence (divergence) over the longitudinal band of 60°–135°E and anomalous descents (ascents) accompanied by zonal wind divergence (convergence) east of 135°E. Different from the coherently dynamical background from 60°E to 160°E in the first EOF

mode, the seasonal-mean divergent flows in the lower troposphere corresponding to EOF2 mode changes sign around 135°E, redistributing the moisture and the associated moist static energy over the Indo-Pacific area, with a significant increase of moist static energy over the southeastern IIO

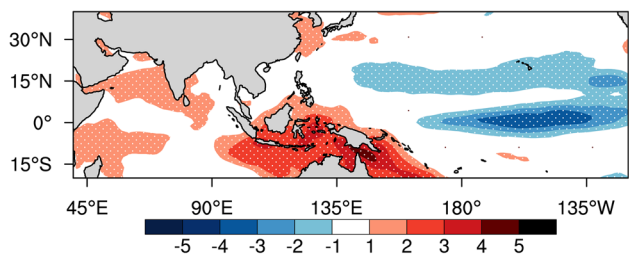


Fig. 15 Differences between strong and weak BSISO years of the second EOF mode of BSISO intensity, in terms of boreal summer seasonal-mean moist static energy averaged between 1000 and 700 hPa (color scale, $J g^{-1}$). Stippling indicates the regions where the differences are statistically significant at the 90% confidence level

and a reduction over the eastern EWP during a La Niña developing summer. Therefore, strong intraseasonal convection are confined mostly to the EIO (Fig. 13a) and fail to continually grow or migrate into the eastern EWP east of 135°E. Opposite situation is for an El Niño developing summer during which anomalous convection mostly develops over the EWP east of 135°E, independent of weak convection signals over the southeastern EIO (Fig. 13b). These indicate that during a La Niña (El Niño) developing summer, the SSTA distribution only favor intraseasonal

convection anomalies over the southeastern EIO (EWP, especially east of 135°E), forming the seesaw pattern of BSISO intensity along the equator.

7 Summary and discussion

The 30–60-day BSISO is an important variability of the ASM, which propagates eastward along the equator, while also moving northward in the SASM region and northward/northwestward in the EA/WNP region. The objective of this study is to identify the dominant spatial and interannual variability of BSISO activity over the entire ASM region, exploring the multi-scale dynamical mechanism and external forcing responsible for the interannual variations of the leading modes of BSISO intensity.

The intraseasonal standard deviations of the 30–60-day filtered GPCP rainfall and OLR are calculated to represent the intensity of the BSISO during each summer for the periods 1981–2014. The dominant spatio-temporal variations of BSISO intensity over the ASM region are identified through EOF analysis. The first EOF mode of the BSISO intensity exhibits a spatially coherent enhancement or suppression of BSISO activity over the entire ASM region, while the second EOF mode is characterized by a dipole structure or

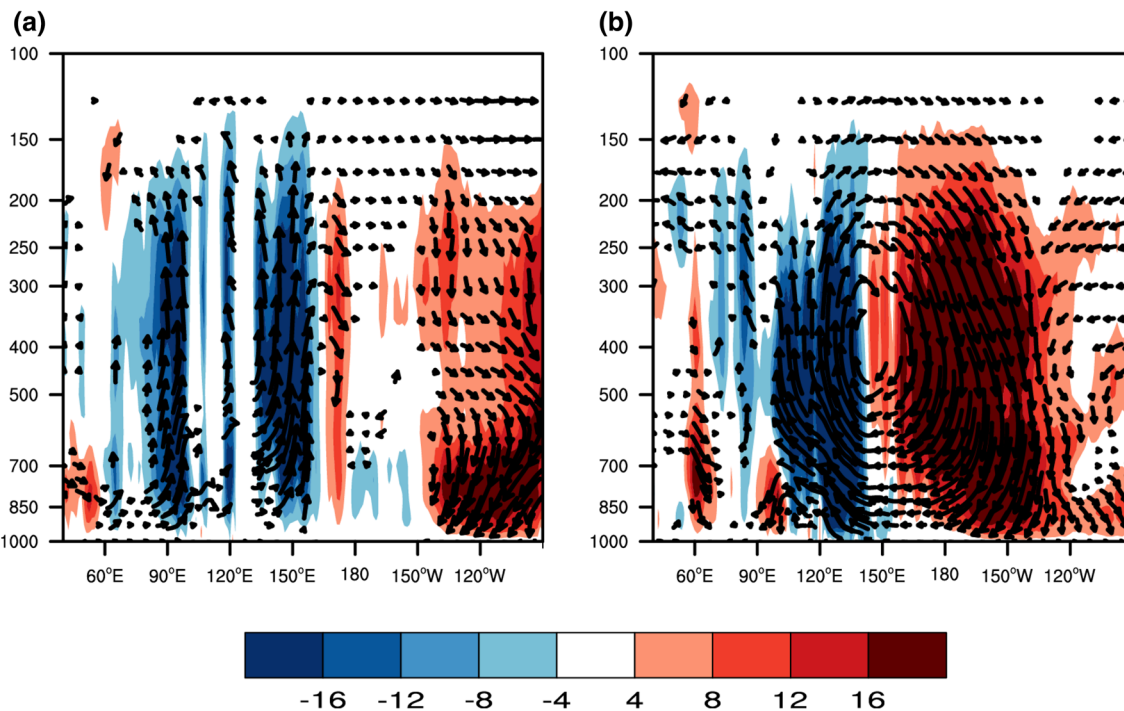


Fig. 16 Pressure–longitude cross sections for differences of boreal summer seasonal-mean equatorial air flows (vectors, zonal wind in $m s^{-1}$ and omega in $10^{-3} \times Pa s^{-1}$) and omega (color scale, $10^{-3} Pa s^{-1}$) between strong and weak BSISO years of the **a** first and **b** sec-

ond EOF mode of BSISO intensity. Vector is displayed only when its zonal or vertical component is statistically significant at the 90% confidence level

seesaw pattern between the southeastern EIO and the EWP. Thus, the standardized PC1 and PC2 time series of the corresponding EOF1 and EOF2 modes derived from OLR are defined respectively as the BIV11 and BIV12 to quantitatively measure the year-to-year variations of BSISO intensity over the ASM region.

Composite analyses are performed to examine the interannual variability for each of the leading two EOF modes of BSISO intensity by comparing the differences in terms of dynamical and thermodynamical variables between anomalously strong and weak BSISO years. For EOF1 mode, significant SSTA contrast between the cooler (warmer) tropical Indian Ocean and the warmer (cooler) CNP is present in strong (weak) years, inducing anomalous low-level westerly (easterly) over the tropical Indian Ocean to the CNP. During strong years, due to the blocking and frictional effect of Maritime Continent, an anomalous cyclonic circulation occurs south of the equator, which leads to a wetter background over the EEIO, thus forming a favorable background for strong intraseasonal convection anomalies. The multi-scale interaction between the wetter background and intraseasonal wind convergence ($\bar{q}\nabla \cdot \bar{V}'$) leads to strong wet anomalies in the PBL over the EEIO in phase 3, thus BSISO-related active convection develops significantly and further propagates to the EWP. The anomalous low-level westerlies also enhance the vertical shear of the seasonal-mean easterly over the western Indian Subcontinent and tropical western Pacific, which further leads to the stronger northward propagation over the SASM and EA/WNP regions through the easterly shear mechanism, respectively. The intensified equatorial active convection anomalies also contribute to the stronger northward propagations over the monsoon regions through moisture mechanism. Therefore, BSISO activities over the entire ASM region are strengthened coherently. Opposite situation is for weak years.

The interannual variation of EOF2 mode of BSISO intensity is found to be closely related to the developing ENSO events. The seesaw patterns with enhanced BSISO activity over the southeastern EIO while weakened activity over the EWP east of 135°E mostly occur in the La Niña developing summers, but opposite seesaw patterns often appear in the El Niño developing summers. In response to the SSTA pattern of La Niña developing phase, an anomalously enhanced Walker Circulation is induced, with seasonal-mean ascents over the southeastern EIO and Maritime Continent but descents over the EWP east of around 135°E. The ascending branch is forced by strong low-level convergence, which further leads to strong moisture convergence over the southeastern EIO and Maritime Continent, accumulating more moist static energy to facilitate strong intraseasonal convection to arise. The BSISO activity thus becomes stronger around the Maritime Continent and its west. Meanwhile, the local

moist static energy over the EWP east of around 135°E is reduced due to the descending background, which restrains the intraseasonal convection to develop, thus the upstream signals are difficult to grow sequentially east of the Maritime Continent, and the intensity of BSISO activity is certainly suppressed. Conversely, the circulation background associated with the El Niño-like SSTA pattern mostly enhances the BSISO activity over the eastern EWP while restrains the activity over the southeastern EIO west of 135°E, forming an opposite dipole pattern to that in La Niña developing summers.

It should be noted that we only link the interannual variations of the two leading EOF modes of BSISO intensity over the ASM region with the simultaneous SSTAs over different basins in summertime. While the interannual variation of EOF2 mode is closely associated with developing ENSO events, what causes the summertime SSTA contrast that modulates the interannual variation of EOF1 mode demands further study. Moreover, Wu and Song (2017) suggests that BSISO intensity shows notable changes between slow and fast decaying El Niño events, indicating that the evolution of SSTA patterns also modulates BSISO behaviors. Thus, how the SSTA patterns in the preceding spring and winter are related to the subsequent summertime SSTAs and their impacts on the BSISO activity need to be further examined. Moreover, the interannual variation of the 10–20-day BSISO over the ASM region and the related mechanisms also need to be investigated in the future.

Acknowledgements This research was jointly supported by the SOA Program on Global Change and Air–Sea Interactions (GASI-IPOVAI-03), the National Natural Science Foundation of China (91537103 and 41730963), the National Basic Research Program of China (2014CB953902), the Priority Research Program of the Chinese Academy of Sciences (QYZDY-SSW-DQC018) and the Fundamental Research Funds for the Central Universities, China University of Geosciences (Wuhan) (CUG170643).

References

- Ajayamohan RS, Rao SA, Yamagata T (2008) Influence of Indian Ocean dipole on poleward propagation of boreal summer intraseasonal oscillations. *J Clim* 21:5437–5454
- Annamalai H, Slingo JM (2001) Active/break cycles: diagnosis of the intraseasonal variability of the Asian summer monsoon. *Clim Dyn* 18:85–102
- Annamalai H, Sperber KR (2005) Regional heat sources and the active and break phases of boreal summer intraseasonal (30–50 day) variability. *J Atmos Sci* 62:2726–2748
- Bellon G, Sobel AH (2008) Instability of the axisymmetric monsoon flow and intraseasonal oscillation. *J Geophys Res* 113:D07108
- Bhat GS (2006) The Indian drought of 2002—a sub-seasonal phenomenon. *Q J R Meteorol Soc* 132:2583–2602
- Bretherton CS, Widmann M, Dymnikov VP, Wallace JM, Blade I (1990) The effective number of spatial degrees of freedom of a time-varying field. *J Clim* 12:1990–2009

- Deng L, Li T, Liu J, Melinda P (2016) Factors controlling the interannual variations of MJO intensity. *J Meteor Res* 30(3):328–340
- Ding QH, Wang B (2009) Predicting extreme phases of the Indian summer monsoon. *J Clim* 22:346–363
- Hoyos CD, Webster PJ (2007) The role of intraseasonal variability in the nature of Asian monsoon precipitation. *J Clim* 20:4402–4424
- Hsu PC, Li T (2011) Interactions between boreal summer intraseasonal oscillations and synoptic-scale disturbances over the western North Pacific. Part II: Apparent heat and moisture sources and eddy momentum transport. *J Clim* 24:942–961
- Hsu PC, Li T (2012) Role of the boundary layer moisture asymmetry in causing the eastward propagation of the Madden–Julian Oscillation. *J Clim* 25:4914–4931
- Huffman GJ, Adler RF, Morrissey M, Bolvin DT, Curtis S, Joyce R, McGavock B, Susskind J (2001) Global precipitation at one-degree daily resolution from multi-satellite observations. *J Hydrometeorol* 2:36–50
- Jiang XA, Li T, Wang B (2004) Structures and mechanisms of the northward propagating boreal summer intraseasonal oscillation. *J Clim* 17:1022–1039
- Jones C, Carvalho LMV, Higgins RW, Waliser DE, Schemm JKE (2004) Climatology of tropical intraseasonal convective anomalies: 1979–2002. *J Clim* 17:523–539
- Kajikawa Y, Yasunari T (2005) Interannual variability of the 10–25- and 30–60-day variation over the South China Sea during boreal summer. *Geophys Res Lett* 32:L04710
- Kemball-Cook S, Wang B (2001) Equatorial waves and air–sea interaction in the boreal summer intraseasonal oscillation. *J Clim* 14:2923–2942
- Kobayashi S, Ota Y, Harada Y, Ebata A, Moriya M, Onoda H, Onogi K, Kamahori H, Kobayashi C, Endo H, Miyaoka K, Takahashi K (2015) The JRA-55 reanalysis: general specifications and basic characteristics. *J Meteorol Soc Jpn* 93:5–48
- Lawrence DM, Webster PJ (2002) The boreal summer intraseasonal oscillation: relationship between northward and eastward movement of convection. *J Atmos Sci* 59:1593–1606
- Lee JY, Wang B, Wheeler MC, Fu XH, Waliser DE, Kang IS (2013) Real-time multivariate indices for the boreal summer intraseasonal oscillation over the Asian summer monsoon region. *Clim Dyn* 40:493–509
- Li J, Mao J (2016) Changes in the boreal summer intraseasonal oscillation projected by the CNRM-CM5 model under the RCP 8.5 scenario. *Clim Dym* 47:3713–3736
- Li RCY, Zhou W (2015) Multiscale control of summertime persistent heavy precipitation events over South China in association with synoptic, intraseasonal, and low-frequency background. *Clim Dyn* 45:1043–1057
- Li C, Jia X, Ling J, Zhou W, Zhang C (2009) Sensitivity of MJO simulations to diabatic heating profiles. *Clim Dyn* 32:167–187
- Li RCY, Zhou W, Li T (2014) Influences of the Pacific–Japan teleconnection pattern on synoptic-scale variability in the western North Pacific. *J Clim* 27:140–154
- Li J, Mao J, Wu G (2015) A case study of the impact of boreal summer intraseasonal oscillations on Yangtze rainfall. *Clim Dyn* 44:2683–2702
- Liebmann B, Smith CA (1996) Description of a complete (interpolated) outgoing longwave radiation dataset. *Bull Am Meteorol Soc* 77:1275–1277
- Liebmann B, Hendon HH, Glick JD (1994) The relationship between tropical cyclones of the western Pacific and Indian Oceans and the Madden–Julian oscillation. *J Meteorol Soc Jpn* 72:401–412
- Lin A, Li T (2008) Energy spectrum characteristics of boreal summer intraseasonal oscillations: climatology and variations during the ENSO developing and decaying phases. *J Clim* 21:6304–6320
- Liu F, Li T, Wang H, Zhang YW (2016) Modulation of boreal summer intraseasonal oscillations over the western North Pacific by ENSO. *J Clim*. <https://doi.org/10.1175/JCLI-D-15-0831.1>
- Madden RA, Julian PR (1971) Detection of a 40–50 day oscillation in the zonal wind in the tropical Pacific. *J Atmos Sci* 28:702–708
- Madden RA, Julian PR (1972) Description of global-scale circulation cells in the Tropics with a 40–50 day period. *J Atmos Sci* 29:1109–1123
- Maloney ED, Hartmann DL (2000) Modulation of eastern North Pacific hurricanes by the Madden–Julian oscillation. *J Clim* 13:1451–1460
- Mao J, Chan JCL (2005) Intraseasonal variability of the South China Sea summer monsoon. *J Clim* 18:2388–2402
- Mao J, Wu G (2010) Intraseasonal modulation of tropical cyclogenesis in the western North Pacific: a case study. *Theor Appl Climatol* 100:397–411
- Mao J, Sun Z, Wu G (2010) 20–50-day oscillation of summer Yangtze rainfall in response to intraseasonal variations in the subtropical high over the western North Pacific and South China Sea. *Clim Dyn* 34:747–761
- North GR, Bell TL, Cahalan RF, Moeng FJ (1982) Sampling errors in the estimation of empirical orthogonal functions. *Mon Weather Rev* 110:699–706
- Qi YJ, Zhang RH, Li T, Wen M (2008) Interactions between the summer mean monsoon and the intraseasonal oscillation in the Indian monsoon region. *Geophys Res Lett* 35:L17704
- Reynolds RW, Smith TM, Liu CY, Chelton DB, Casey KS, Schlax MG (2007) Daily high-resolution-blended analyses for sea surface temperature. *J Clim* 20:5473–5496
- Saji NH, Goswami BN, Vinayachandran PN, Yamagata T (1999) A dipole mode in the tropical Indian Ocean. *Nature* 401:360–363
- Seo KH, Wang SchemmJ-KE, Kumar W A (2007) The boreal summer intraseasonal oscillation simulated in the NCEP Climate Forecast System (CFS): the effect of sea surface temperature. *Mon Weather Rev* 135:1807–1827
- Tao SY, Chen L (1987) A review of recent research on the onset Asian summer monsoon in China, In: Chang CP, Krishnamurti TN (eds) *Monsoon Meteorology*. Oxford University Press, Oxford, pp 60–92
- Teng HY, Wang B (2003) Interannual variations of the boreal summer intraseasonal oscillation in the Asian–Pacific Region. *J Clim* 16:3572–3584
- Tong HW, Chan JCL, Zhou W (2009) The role of MJO and mid-latitude fronts in the South China Sea summer monsoon onset. *Clim Dyn* 33:827–841
- Trenberth KE (2011) Changes in precipitation with climate change. *Clim Res* 47:123–138
- Wang B, Rui H (1990) Synoptic climatology of transient tropical intraseasonal convection anomalies: 1975–1985. *Meteorol Atmos Phys* 44:43–61
- Wang B, Xie X (1997) A model for the boreal summer intraseasonal oscillation. *J Atmos Sci* 54:72–86
- Webster PJ, Magana VO, Palmer TN, Shukla J, Tomas RA, Yanai M, Yasunari T (1998) Monsoons: processes, predictability, and the prospects for prediction. *J Geophys Res* 103(C7):14451–14510
- Wu RG, Cao X (2016) Relationship of boreal summer 10–20-day and 30–60-day intraseasonal oscillation intensity over the tropical western North Pacific to tropical Indo-Pacific SST. *Clim Dyn*. <https://doi.org/10.1007/s00382-016-3282-5>
- Wu RG, Song L (2017) Spatiotemporal change of intraseasonal oscillation intensity over the tropical Indo-Pacific Ocean associated with El Niño and La Niña events. *Clim Dyn*. <https://doi.org/10.1007/s00382-017-3675-0>
- Yanai M, Esbensen S, Chu J-H (1973) Determination of bulk properties of tropical cloud clusters from large-scale heat and moisture budgets. *J Atmos Sci* 30:611–627

- Yang J, Wang B, Wang B (2008) Anticorrelated intensity change of the quasi-biweekly and 30–50-day oscillations over the South China Sea. *Geophys Res Lett* 35:L16702
- Zhou W, Chan JCL (2005) Intraseasonal oscillations and the South China Sea summer monsoon onset. *Int J Climatol* 25:1585–1609
- Zhu C, Nakazawa T, Li J, Chen L (2003) The 30–60 day intraseasonal oscillation over the western North Pacific Ocean and its impacts on summer flooding in China during 1998. *Geophys Res Lett* 30(18):1952